Chapter 3
Computational Methodology

The approach of this research effort was to employ a commercial optimization software package in conjunction with a computational fluid dynamics (CFD) package in the design and optimization of a leading edge fillet for a turbine vane. CFD has been shown by many researchers to be an effective and efficient design tool, and implementation of automated optimization algorithms in the CFD design process is a logical next step. As there were no known integrated optimization/CFD packages, a large portion of this research effort was devoted to such an integration. After performing a proof-of-concept optimization to verify code integration, this approach was successfully applied to a preliminary fillet design test case. Through the preliminary fillet optimization, it was learned that the optimization algorithms utilized resulted in excessive computational time and expense. Due to the excessive amount of time to optimize, Design of Experiments (DOE) using Orthogonal Arrays was employed in subsequent optimization efforts. The results of all optimization efforts and DOE studies are presented in Chapter 5.

This chapter presents the details of the computational and optimization approach taken in this research. First, a brief description of the computational codes utilized will be given, followed by a discussion of the fluid dynamics modeling and optimization algorithms employed. Next, details of the integration of the optimization shell and CFD package will be presented. In the following section, the computational solution domain and vane geometry will be presented along with the boundary conditions applied in the simulations. Subsequently, the mathematical models of the leading edge fillet, which define the design parameters for the optimization effort, will be presented, followed by a brief discussion of the objective function selection process. Finally, details of the thermal and secondary flow analyses used to visualize the impact of the fillet on the flow will be presented.

3.1 Computational Codes

The CFD package chosen for this study is a product of Fluent, Inc. and consists of a preprocessor called GAMBIT and a suite of flow solvers tailored to various flow

situations (Fluent, 1998). The flow solver used in this investigation is FLUENT 5 version 5.1, while version 1.1 of the GAMBIT preprocessor was utilized. There were several fundamental reasons for the selection of this CFD package, foremost among which are successful benchmarking of the code against experimental flow data taken in the vane passage, a built-in comprehensive set of turbulence models, the ability to mesh complex geometries using unstructured meshing techniques, and solution-based mesh adaption.

The GAMBIT preprocessor, introduced into the Fluent CFD package in 1998, provides a single user-friendly interface for geometry creation, mesh generation, and mesh quality diagnostics. In this research, GAMBIT was utilized in defining the solution domain, generating a suitable computational mesh, and specifying boundary types. Perhaps the most valuable asset to the current investigation is the journaling capability of GAMBIT which allows for parametric geometry definition. This capability enabled automated alterations to the leading edge fillet geometry and reliable meshing of the solution domain.

The flow solver used in this investigation is FLUENT 5. FLUENT 5 represents the integration and extension of two previously separate solvers, FLUENT/UNS and RAMPANT 4.2. The combined solver is capable of handling flow problems ranging from incompressible to hypersonic with its various solver formulations and discretization schemes. Fluent 5 provides both segregated-implicit and coupled-explicit/implicit solver formulations, all based on the finite volume method. In addition, FLUENT 5 offers complete unstructured mesh flexibility, non-conformal mesh interface capabilities, and solution-based mesh adaption, making it ideal for applications involving complex flow geometry. For its ability to handle an unstructured mesh, FLUENT 5 was selected for flow computations in this investigation.

The optimization software employed in this investigation is a product of Engineous Software, Inc. called iSIGHT (Engineous Software, Inc., 1999). Version 5.0 of iSIGHT was used in this investigation. iSIGHT is an optimization shell that essentially functions as the design engineer in the design-evaluate-redesign cycle, freeing the engineer from the repetitive tasks involved in this process. In addition to automating design tasks, iSIGHT enables the integration of multiple simulation codes and

engineering intelligence into a common framework, allowing for true multidisciplinary design optimization. To drive the investigation of design alternatives, iSIGHT offers a variety of optimization algorithms that are grouped into three main categories: numerical, exploratory, and expert system or knowledge-based techniques. In addition to the many optimization techniques, Design of Experiments (DOE) is also incorporated in the software. DOE provides a systematic and efficient means of analyzing a design space, allowing for design variable screening, assessment of design variable impact, and evaluation of significant design variable interactions. The full benefit of iSIGHT is realized through the seamless integration and automation of these techniques into the design process.

3.2 Computational Fluid Dynamics Modeling

All computational simulations performed in this investigation were for low-speed, incompressible wind tunnel conditions. Low-speed, large-scale conditions allowed for matching of the inlet Reynolds number with engine conditions, however, the Mach number distribution about the airfoil was not matched. While the tested turbine vane geometry is a transonic design, the maximum Mach number of the flow in the computational simulations and in the wind tunnel never exceeded Ma = 0.1. Given the negligible compressibility effects on the flow field, the flow was modeled as an incompressible ideal gas in all simulations. In Fluent, this model calculates the local density, ρ, from the local temperature, T, and a fixed operating pressure, p_{oper}, as

$$\rho = \frac{p_{oper}}{RT} \tag{3.1}$$

where R is the gas constant for air. The operating pressure for all simulations was set to typical local atmospheric pressure, which in Blacksburg, VA is approximately 95 kPa. Since the simulated low-speed conditions result in relatively small changes in static pressure (<800 Pa) throughout the vane cascade, the pressure field does not have a large impact on the calculated density, making the assumption of a constant operating pressure reasonable. In contrast, the modeled temperature distribution through the cascade does

have a significant effect on the density field. For this reason, the local density is calculated using local temperature. The specific heat, c_p, and thermal conductivity, k, of air were modeled as constant in all simulations. Though these fluid properties are functions of temperature, the range of flow temperatures modeled was relatively low, making the assumption of constant properties reasonable. The absolute viscosity, μ, of air was also modeled as constant except in the preliminary optimization effort, where the range of flow temperatures was large. In these simulations, the temperature dependence of absolute viscosity was modeled using the empirical correlation of Sutherland (1893).

The set of equations solved in each simulation included the continuity equation, the Reynolds-averaged Navier-Stokes equations (x, y, and z momentum), the energy equation, and the chosen turbulence model equations. All simulations were calculated using the steady-state segregated, implicit solver formulation. This formulation employs a pressure-correction scheme whereby the momentum equations are solved sequentially for the velocity components using the best available estimate for the pressure distribution. Subsequently, the pressure correction is calculated from a derived Poisson equation, and the process is repeated until the continuity equation is satisfied. The pressure-correction scheme utilized for the simulations reported herein was developed by Patankar (1980) and is called SIMPLE (Semi-Implicit Method for Pressure-Linked Equations). The SIMPLE algorithm provides the necessary coupling between the calculated velocity field and the pressure field for segregated solution of the governing equations. Second-order discretization of the governing equations was used for all computations.

Reynolds-averaging the Navier-Stokes and energy equations results in the formation of additional terms that represent the effects of turbulence transport. These additional terms are referred to as the Reynolds stresses in the momentum equations and the Reynolds heat flux term in the energy equation, and for closure of the equation set, they must be modeled in some way. Fluent provides many different turbulence models from which to choose, including the standard k-ε model (Launder and Spalding, 1974), the realizable k-ε model (Shih et al., 1995), the Renormalization Group (RNG) k-ε model (Yakhot et al., 1992), the Spalart-Allmaras model, and the Reynolds Stress Model (RSM) (Launder et al., 1975).

In selection of a turbulence model, a decision regarding treatment of the near-wall region also has to be made as most models are primarily valid only for turbulent core flows far from walls. There are two approaches to modeling the near-wall region in Fluent. The first approach is to model all the way to the wall with a mesh of sufficient resolution to resolve the boundary layer. Typically, this approach requires the first grid point from the wall to be within a $y^+ = 1$, and at least 5 grid points to be within the viscous sublayer. Given these mesh requirements, it is easy to conceive that this approach involves a considerably large amount of computational expense. Of the turbulence models offered in Fluent, the Spalart-Allmaras model is the only model specifically designed for application throughout the boundary layer. The second approach to modeling the near-wall region is to use semi-empirical formulas called "wall functions" to bridge the gap between the wall and fully-turbulent region. The use of wall functions eliminates the near-wall meshing requirements associated with modeling to the wall and the concern of turbulence model applicability within the boundary layer. Due to the savings in computational expense, wall functions were employed in this investigation to model the near-wall region.

Fluent provides two different wall function formulations, standard equilibrium wall functions and nonequilibrium wall functions. For an equilibrium or zero pressure gradient flow, standard wall functions are appropriate; however, in flows with large pressure gradient, nonequilibrium wall functions will model the near-wall region better. Given the significant amount of flow acceleration through the vane passage, non-equilibrium wall functions were utilized in all simulations. The general approach in the development of nonequilibrium wall functions has been to start with the standard law-of-the-wall for mean velocity and to then sensitize the equation to pressure gradients. This was the approach taken for the non-equilibrium wall functions available in Fluent (Kim and Choudhury, 1995). The law-of-the-wall for temperature is derived from that for mean velocity using Reynolds' analogy between momentum and energy transport and assuming equilibrium flow. The thermal law-of-the-wall remains unchanged with application of nonequilibrium wall functions.

The turbulence model selected for the current investigation is the RNG k-ε model (Choudhury, 1993). For this k-ε model, equations for k and ε are derived through

application of a rigorous statistical technique called Renormalization Group theory to the instantaneous Navier-Stokes equations. This means of development differs from that of the standard k-ε model, which is derived from the Reynolds-averaged equations, and gives rise to an additional term in the model equation of turbulence dissipation. With this additional term, the RNG k-ε model has been found to better predict situations with significant streamline curvature such as separated flows, recirculating flows, and endwall secondary flows. In a study by Hermanson and Thole (1999), the predictive capabilities of the standard k-ε and RNG k-ε models were benchmarked against experimental velocity data taken by Kang et al. (1998) in the stagnation plane of a turbine vane. Calculations using the standard k-ε model yielded a poor prediction of the leading edge vortex shape and location, while use of the RNG k-ε model was found to provide excellent agreement to experimental measurements as shown in Figure 3.1. In addition to providing an accurate prediction of the leading edge vortex shape and location, the RNG k-ε model also predicted vorticity magnitude quite well, closely matching experimental results. Since the investigation reported herein uses the same turbine vane geometry, the RNG k-ε turbulence model was selected for closure based on the predictive success of Hermanson and Thole.

3.3 Optimization Methods

iSIGHT provides many optimization techniques from which the user can choose. These techniques are categorized into three main groups: numerical techniques, exploratory techniques, and expert system techniques. The available numerical techniques include: Modified Method of Feasible Directions-ADS (Automated Design Synthesis), Method of Feasible Directions-CONMIN (Constrained Function Minimization), Sequential Linear Programming, Sequential Quadratic Programming-ADS, Sequential Quadratic Programming-DONLP (Differentiable Nonlinear Programming), Successive Approximation Method, Exterior Penalty, Augmented Lagrangian, and the Hooke-Jeeves Direct Search Method. Numerical techniques generally assume that the design space is convex, continuous, and unimodal. Because of this, numerical techniques tend to converge quickly to a local optimum close to the initial design point. Thus, the effectiveness of numerical optimization techniques in finding a

global optimum is highly dependent on the topology of the design space and the choice of initial design point. Available exploratory techniques include: Genetic Algorithm, Genetic Algorithm with Bulk Evaluation, and Simulated Annealing. These techniques avoid a concentrated search in a local region of the design space. Instead, exploratory techniques evaluate designs throughout the design space in search of a global optimum. iSIGHT provides only one optimization technique, called Directed Heuristic Search, in the expert system category. Directed Heuristic Search follows user-defined directions on what design variables to change, when to change them, and by how much. This allows the user to incorporate real-world design knowledge to increase the efficiency of the optimization process.

Though at the time of this investigation, Simulated Annealing and Genetic Algorithm were the only global optimization techniques incorporated into the iSIGHT framework, several more modern global techniques are worthy of note. While both methods mentioned above are motivated by observed processes in nature, these processes are not necessarily the most efficient. Modern global optimization algorithms excel in efficiency through planned, intelligent exploration of the design space. One such modern method called DIRECT, short for "DIviding RECTangles", is particularly effective in finding the global optimum for problems with widely separated local optima. DIRECT is a modified Lipschitzian optimization algorithm that does not require specification of the Lipschitz constant, first presented by Jones et al. (1993). Cox et al. (2001) performed a study comparing the effectiveness of DIRECT with two other multistart global optimization approaches in the design of a high-speed civil transport. For a small number of design variables, one of the multistart methods proved to be most efficient; however, as the number of design variables was increased, the effectiveness of the multistart methods deteriorated faster than that of DIRECT. The reason for this trend is that the number of separated optima can increase exponentially with problem dimensionality, a situation for which DIRECT is particularly well suited. More comprehensive coverage of global optimization techniques and deterministic methods in particular is given by Floudas (1999).

Since it is usually advantageous to employ multiple techniques in the optimization process, iSIGHT allows the user to combine optimization techniques into an optimization

plan. For example, the most efficient or optimum optimization plan for a given problem may begin with an exploratory technique and then transition to a numerical technique. Unfortunately, there is no means of determining what constitutes the most efficient optimization plan a priori. In addition, the most efficient optimization plan is highly dependent on the particular problem being solved. For the preliminary fillet design effort, Simulated Annealing was used to initiate the optimization process. The primary reason for starting with Simulated Annealing was to avoid convergence to a local optimum in the vicinity of the initial design point, the Achilles' heel of most numerical techniques. In addition, as the initial stages of Simulated Annealing are devoted to global diffuse searching, the technique lends itself to design space exploration. Upon completion of the exploration runs, the intent was to switch to a gradient-based technique, specifically Modified Method of Feasible Directions, starting from the best design point among those evaluated under Simulated Annealing. For some reason, possibly an iSIGHT coding error, the intended switch did not occur.

Simulated Annealing derives its name from the physical process of annealing, whereby a brittle metal is toughened through heating followed by slow controlled cooling. Similar to the physical process, Simulated Annealing is based on a temperature schedule that dictates the search for a global optimum. To visualize the optimization process, it is helpful to draw an analogy to a bouncing search ball in a mountainous design space where the objective is to find the global minimum. At the start of the optimization process, the temperature is the highest, enabling the search ball to bounce over any mountain and thereby access any valley. The high energy of the ball leads to global diffuse searching at the outset of the optimization. It is this characteristic of Simulated Annealing that was attractive in the current investigation. As the temperature decreases throughout the process, the ball's energy level and therefore its bounce also decrease, resulting in a statistical reduction of the search domain. Ultimately, Simulated Annealing concludes with a local focused search prior to convergence to the global optimum.

Among the attractive features of Simulated Annealing are its ability to handle objective functions with arbitrary degrees of nonlinearity and discontinuities while statistically guaranteeing determination of the true global optimum. Unfortunately,

Simulated Annealing can be excessively time-consuming, which, in practice, has led to the use of temperature schedules too fast to satisfy the sufficiency conditions of the technique. For standard Boltzmann Simulated Annealing a logarithmic temperature schedule is required to guarantee convergence to the global optimum. However, for reasons of expediency, many researchers have used an exponential temperature schedule with the algorithm. These modified faster algorithms are more aptly referred to as Simulated Quenching and do not statistically guarantee determination of the global optimum. The specific formulation of Simulated Annealing incorporated into iSIGHT is the Adaptive Simulated Annealing algorithm authored by Lester Ingber (1989). Adaptive Simulated Annealing differs in formulation from the standard Boltzmann algorithm, allowing for exponential temperature schedules while maintaining a statistical guarantee of convergence to the global optimum. In addition, Adaptive Simulated Annealing has the ability to recursively optimize algorithm parameters, thereby speeding convergence.

The intended gradient-based optimization technique is the Modified Method of Feasible Directions-ADS, whereby the algorithm proceeds in the direction of maximum ascent or decent. If the design space is characterized by multiple local optima, the optimum found will be highly dependent on the initial starting point in parameter space. An analogy to this technique is a near-sighted mountain climber that is so focused on the local mountain that the mountain range and global optimum are overlooked. If the design space is characterized by a single peak, this technique is extremely efficient. However, this extent of design space knowledge is usually unavailable at the outset of an optimization, in which case the Modified Method of Feasible Directions should be applied with caution. In the next section of this chapter, the results of an optimization problem formulated to test the integration of Fluent and iSIGHT will be presented for which the Modified Method of Feasible Directions was utilized. The proof-of-concept problem was known to have a design space with a single peak and was selected for this reason.

From the results of the preliminary fillet optimization effort, it became apparent that the optimization algorithm was driving the design to near-maximum fillet dimensions. In light of this observation and the significant computational expense involved in the optimization process, a new approach was considered for subsequent

optimization efforts in the hope of reducing the time to optimize. The new approach was to use Design of Experiments (DOE) for design space exploration and to create a Response Surface Model (RSM) from the results of the DOE study. A RSM is essentially a curve fit of the available data, in this case, the DOE results. The RSM could then be used for optimization, with the benefit of greatly reduced evaluation time and computational expense. Upon arriving at an optimum, iSIGHT could run a full CFD simulation and use the results to update the RSM. With each iteration of this process, the RSM would become increasingly more accurate in the region about the optimum. When the optimum design point no longer varied as determined using the RSM, the process would terminate. Ultimately, this technique was not fully employed for several reasons. First, at the time of this work, iSIGHT did not have integrated RSM capabilities, and establishing such an integration would have required significant additional time and effort. The second and most compelling reason is that the results of an initial DOE study indicated rather simplistic design space topology. Determination of the optimum or very nearly the optimum could be made visually from a contour plot of the DOE results.

3.4 Integration of Optimization and CFD Packages

Prior to discussing the specifics of the integration of iSIGHT and Fluent, it is instructive to consider how iSIGHT works in a generic sense. As an optimization shell, iSIGHT is designed to run simulation codes that are executed from the command line and use structured text files as input and output. Through iSIGHT's file parsing capability, the results of a simulation can be retrieved from the output file(s), stored, and evaluated. Based on the simulation results and the goals of the optimization, iSIGHT then modifies the design parameters in the input file and runs the simulation code again. This process continues until iSIGHT converges on an optimum design. Guided by the problem definition and optimization plan, iSIGHT automates simulation code execution, data retrieval, and iterative adjustment of the design parameters. In this way, iSIGHT replaces the design engineer in the design-evaluate-redesign cycle as shown in Figure 3.2.

To link iSIGHT with the Fluent CFD package, extensive use was made of the journaling features of FLUENT 5 and the preprocessor, GAMBIT. Journaling allows for the creation of simple text files that contain a sequential set of program commands that

are to be executed. These journal files can then be specified as input to the simulation code and executed from the command line. The GAMBIT journal file contains all the commands for geometry creation and meshing of the solution domain, while the FLUENT 5 journal files contain the commands for reading in the mesh file, specifying the solver settings and discretization schemes, selecting turbulence and fluid property models, partitioning for solution on multiple processors, and ultimately initiating solution iteration. Thus, the journal files for GAMBIT and FLUENT 5 served as the simulation code input files, as indicated in Figure 3.2. Using the file parsing capabilities of iSIGHT, design parameters specified in these files were automatically altered between design iterations.

Since the goal of the computational design was to optimize fillet shape, the fillet geometry and therefore the solution domain had to be altered between CFD runs. This was achieved by creating a parametric model of the leading edge fillet and applying the model to geometry creation within the GAMBIT journal file. Fortunately, the journaling capabilities of GAMBIT allow for the specification of parameters and the use of parameters in mathematical expressions. By specifying these geometric parameters to be design variables, iSIGHT has the ability to alter the shape of the fillet between simulation runs. The parametric description of the leading edge fillet is presented in section 3.6 of this chapter.

Of particular importance in this investigation was the automation of model and mesh generation using GAMBIT. Extreme care had to be taken in development of the GAMBIT journal file. Since GAMBIT has a hierarchal structure whereby surfaces are defined by edges and edges are defined by points, it was extremely important to maintain a rigid order of operations for both geometry creation and mesh generation. Any change to the order of operations would result in certain error and the propagation of such through the entire model creation process. For mesh generation, proper specification of node distributions along the edges of the domain was critical to ensure creation of a suitable mesh. Since the fillet geometry varied from simulation to simulation, the associated lengths of edges also varied, making it requisite that the applied meshing procedures account for these geometric changes. On the endwall, fillet, and vane surfaces, the node spacing was specified to be 0.004 m (0.7% S), while spacing was

relaxed into the freestream. This spacing results in appropriate y^+ values, between approximately 30 and 60, for application of wall functions. Node spacing was also relaxed on the downstream portion of the endwall approaching the exit plane of the solution domain. A typical solution domain, as described in section 3.5, consisted of approximately 800,000 to 900,000 cells depending on the size of the fillet. Solution-based mesh adaption was employed to ensure grid independence for the automatically generated meshes. Adaptions based on y^+ and temperature gradients were performed resulting in an adapted cell count of 1.2 million. Results for the adapted mesh indicated negligible change to the calculated thermal field, leading to the conclusion that the automated meshing process was sufficient.

Ultimately, the simulation code for the preliminary optimization effort was an executable script file containing the commands to run GAMBIT and FLUENT 5 with the corresponding journal files specified as input. In addition to running these codes, the executable script file contained several UNIX commands to manage the output files. Appendix A contains the FLUENT 5 journal files in their entirety, and the executable script described above. Excerpts from the GAMBIT journal file are also included in Appendix A, as in its entirety the journal file is in excess of 100 pages.

To evaluate the relative performance of a design, a simulation code must produce an output file or files containing the optimization objective function. Fortunately, FLUENT 5 has tremendous flexibility in defining output variables and allows the user to write variables to a file as the solution converges. Both of these operations were included in the FLUENT 5 journal files. Using the file parser in iSIGHT, the objective function was retrieved from the output file, recorded and evaluated as illustrated in Figure 3.2.

Simulations were performed on either a Silicon Graphics Origin2000 or a Silicon Graphics 2100. The Origin2000 is a 32 processor high-end computing system housed in Virginia Tech's Interdisciplinary Center for Applied Mathematics (ICAM), while the 2100 is a 4 processor machine located in the Virginia Tech Experimental and Computational Convection Laboratory. Computations were typically performed in parallel on four processors to minimize wall clock time for solution convergence. To initiate the parallel solver, the solution domain was first partitioned into four solution zones of nearly equivalent cell count. The time required for execution of the GAMBIT

journal file, written to automate model generation and meshing of the solution domain, was approximately 25 CPU minutes. With the generated grid consisting of 800,000 to 900,000 cells, solution convergence was achieved in 705 iterations with better than four orders of magnitude drop in the residuals. Performing the calculations in parallel on four processors, solution time was approximately 10 wall clock hours or 40 CPU hours. In the preliminary optimization effort, additional time was required for calculation of the objective function after each iteration. As the objective function was an integral quantity, the computation time was substantial and nearly doubled the solution time. Realizing the computational expense of these calculations, the objective function was not calculated after every iteration in subsequent simulations. In comparison to the time required for a CFD simulation, the time requirement of iSIGHT was negligible.

To confirm successful integration of Fluent and iSIGHT, a simple proof-of-concept optimization was performed. The problem selected for this demonstration was flow about a symmetric NACA 0012 airfoil at varying angle of attack, α. For a specified range of the design variable, which in this case was the angle of attack, an optimization study was performed with the goal of maximizing the coefficient of lift, C_L, as defined in equation 3.2,

$$C_L = \frac{F_L}{\frac{1}{2}\rho V^2 A_P} \tag{3.2}$$

where the lift force, F_L, is defined normal to the flow direction and A_P is the projected area of the airfoil onto a plane perpendicular to the lift vector. Though this proof-of-concept problem is not design optimization in a precise sense, it was sufficient in demonstrating code integration with the additional benefit of knowledge of the design space. Most undergraduate fluid mechanics textbooks include discussion of the lift characteristics of simple airfoil shapes at varying angle of attack. The coefficient of lift is known to increase nearly linearly with increasing angle of attack until the onset of flow separation on the airfoil suction surface. As the separated flow region increases in size covering most of the suction surface, the airfoil is said to be stalled. The result of stall is considerable loss of lift and thus a significant drop in the coefficient of lift. In the proof-

of-concept optimization, the angle of attack was constrained between 4° and 9° to preclude such flow separation and loss of lift. The airfoil was flown at atmospheric pressure and a freestream Mach number of 0.4. Starting at an angle of attack of 6°, the Modified Method of Feasible Directions was selected to direct the optimization. The convergence history is plotted in Figure 3.3 in the form of angle of attack versus optimization run counter. It is interesting and worthy of note that the optimization process continued beyond the optimum design. The reason for this is that the optimizer must validate the optimum before it can claim it as such. The resulting coefficient of lift versus angle of attack is plotted in Figure 3.4.

3.5 Turbine Vane Geometry and Simulation Boundary Conditions

The turbine vane geometry used in this research is from a Pratt & Whitney advanced, commercial, high-pressure turbine. For wind tunnel testing, the vane geometry was scaled up by a factor of nine to allow for high spatial resolution flow measurements. Development of the large-scale cascade has been thoroughly documented by Kang and Thole (2000) and Radomsky and Thole (2000). The vane coordinates, supplied by Pratt & Whitney and included in Appendix B, represent a two-dimensional slice through the vane midspan. In all three-dimensional computational simulations, this two-dimensional vane profile was assumed for all radial distances. In addition, for consistency with the experimental linear cascade, the vane flow passage was modeled as linear (i.e. at an infinite radial position). Though this does not perfectly model the actual vane, simplified models such as these provide valuable insight into the various mechanisms that dictate the flow field. Table 3.1 presents a comparison of the vane operating conditions in the engine at design altitude of 9.1 km with the vane model operating conditions in the wind tunnel. As was mentioned earlier, the vane scaling enabled matching of Reynolds number but not Mach number. All geometric characteristics such as aspect ratio (C/S), solidity ratio (C/P), and inlet and exit flow angles remained unchanged.

An illustration of the baseline computational domain used for the preliminary optimization effort is given in Figure 3.5. For the baseline case, a relatively small fillet was placed at the junction between the vane and endwall to model a manufacturing fillet typical of current turbine design practice. Previous computational work by Hermanson

(1999) showed that such a small manufacturing fillet has negligible impact on the secondary flow field that develops. The inlet of the solution domain is located one chord upstream of the vane dynamic stagnation point to eliminate the vane's influence on the applied inlet boundary conditions. Placement of the inlet boundary at this distance was determined from the upstream influence of the vane as calculated by Hermanson (1999). Figure 3.6 presents normalized profiles of streamwise velocity, U/U_{inlet}, versus pitchwise location as predicted by CFD at various distances upstream of the vane leading edge. From these plots of streamwise velocity, it can be seen that the vane begins to influence the velocity field as far upstream as 0.6C.

The vane is split at the dynamic stagnation with the suction side defining one face of the domain and the pressure side defining another face. The exit of the domain is located 1.5 chords from the vane trailing edge in the exit flow direction of 78.0 degrees. In order to prevent highly skewed cells at the exit of the domain, an additional 0.1 chord was added in the axial direction. To model an infinite linear cascade, the lateral surfaces between the vane dynamic stagnation and inlet as well as the lateral surfaces between the vane trailing edge and exit were modeled as periodic. A symmetry boundary condition was applied at the vane midspan to reduce computational expense. The endwall, fillet, and vane surfaces were modeled as adiabatic to permit comparison to experimental results of adiabatic wall temperature. In the experimental phase of this investigation, non-uniform temperature profiles, generated by an upstream combustor simulator, were considered at the inlet to the vane cascade, and the redistribution of the flow was evaluated through thermal field and surface temperature measurements. To enable measurement of adiabatic wall temperature, the endwall and vane surfaces were constructed of low thermal conductivity foams. As the objective of the leading edge fillet is to improve the thermal environment throughout the vane passage, the distribution of adiabatic wall temperature is indicative of fillet performance. The fillet optimization/design process was therefore guided by the minimization of adiabatic wall temperature distribution on the vane and endwall surfaces, as is discussed in section 3.7 of this chapter.

A representative filleted solution domain for the preliminary optimization effort is shown in Figure 3.7. In comparison with the baseline domain, the leading edge fillet

designs considered are shown to represent a significant departure from current turbine design practice. To simplify the geometry creation process, the fillet profile shape for the preliminary optimization was chosen to be linear. In subsequent optimization efforts which include a backward-facing slot directly upstream of the vane leading edge, interference issues between the slot and linear fillets led to investigation of fillets with elliptical profile shape. An illustration of the vane leading edge region including the backward-facing slot and an elliptical fillet is given in Figure 3.8. The key features of the solution domain such as the locations of the inlet and outlet remained unchanged throughout all computational studies.

Numerous inlet boundary conditions were considered in the computational design of the leading edge fillet. To clearly present the evolution of the fillet design process, these boundary conditions are presented in the order of their application. For the preliminary fillet optimization, the applied inlet boundary conditions were rather simplistic and are not entirely representative of the conditions exiting a typical engine combustor. Nonetheless, the preliminary boundary conditions were a reasonable starting point and valuable insight into fillet design was obtained in the process. In subsequent fillet optimization efforts, it was desired to more accurately represent typical engine inlet conditions to the vane. To achieve this experimentally, a combustor simulator was designed and constructed upstream of the vane cascade to reproduce the fluid dynamics of a typical engine combustor. For computational design purposes, experimental measurements at the exit of the combustor simulator were used to develop inlet boundary conditions for fillet optimization, with the intention of optimizing at these conditions and ultimately verifying fillet performance experimentally. Of particular importance was specification of the total pressure profile at the inlet to the cascade, since this profile dictates secondary flow development and the associated redistribution of the flow. Expressed nondimensionally by equation 3.3, the measured total pressure distribution at the exit of the combustor simulator is consistent with the experience of Pratt & Whitney and therefore is believed to be representative of typical engine conditions.

$$\Delta p_o = \frac{p_o - p_{o,ms,ave}}{\frac{1}{2}\rho U_{ave}^2} \tag{3.3}$$

A second important boundary condition to accurately specify was the inlet temperature profile. Though the inlet temperature profiles achievable with the combustor simulator are obviously much less severe than typical engine conditions, the generated profiles present an adequate temperature differential for thermal field and endwall adiabatic effectiveness measurements. Expressed in nondimensional form by equation 3.4, the temperature profiles at the exit of the combustor simulator are a reasonable match to typical engine conditions.

$$\theta' = 1 - \theta = \frac{T - T_c}{T_{ms} - T_c} \tag{3.4}$$

In equation 3.4, T_{ms} and T_c are the midspan and coolant temperatures, respectively. For analysis of computational results, the midspan temperature, T_{ms}, was in all cases the maximum temperature in the applied inlet temperature profile. The coolant temperature, T_c, however was not assumed to necessarily correspond with the minimum profile temperature, T_{min}. By physical argument, T_{min} has to be greater than or equal to T_c due to inherent mix-out of the coolant. In the analysis of experimental results, T_{ms} was taken to be the temperature as sensed by a thermocouple mounted at the midspan and dynamic stagnation of the center vane in the cascade, while T_c was taken to be the temperature as measured in the supply chamber of the last combustor cooling panel. To enable comparison of the computational and experimental results, the computational value of T_c was used as a "tuning" parameter to nondimensionally match the temperature profiles at the inlet to the vane. By assuming different values of T_c, the nondimensional temperature distribution at the inlet to the vane passage could be altered to match experimental measurements. In all simulations, the inlet boundary conditions were assumed to be uniform in the pitchwise (circumferential) direction. The key characteristics as well as a description of each inlet boundary condition applied in the computations are tabulated in Table 3.2.

The inlet boundary conditions for the preliminary fillet optimization effort (Case 1) were adapted from previous work by Hermanson (1999). Hermanson used a two-

dimensional boundary layer code called TEXSTAN (Crawford, 1994) to generate spanwise (radial) profiles of velocity, turbulent kinetic energy, and turbulence dissipation rate for different turbulent boundary layer thicknesses entering the vane cascade. The profiles used for the preliminary optimization effort were for a boundary layer thickness of 9.1% span and are presented in nondimensional form in Figures 3.9 through 3.11. Superimposed onto these profiles, a scaled temperature profile, spanning 126 K, was also applied at the inlet. The temperature profile, expressed nondimensionally by equation 3.4 and presented in Figure 3.12, was supplied by Pratt & Whitney and is supposed to be representative of that exiting a typical combustor. As no value of T_c was explicitly stated for this temperature profile, T_c was assumed to be equal to T_{min}. Figure 3.13 is a plot of the resultant nondimensional total pressure profile, Δp_o. Interestingly, the superimposed temperature profile gives rise to a peak in total pressure in the near wall region. The reason this peak occurs is that the density of the near wall fluid is greater due to the lower temperatures. Thus, the dynamic pressure of the near wall fluid exceeds that of the freestream fluid and results in a total pressure peak. For comparison, the total pressure profile assuming an isothermal turbulent boundary layer is plotted in Figure 3.14. The total pressure profile exiting an actual combustor is believed to feature a peak near the wall, and measurements at the exit of the combustor simulator used in this investigation substantiate that belief. Though the preliminary optimization boundary conditions feature a peak in total pressure, the peak is less significant and overall much broader in the spanwise direction compared to that observed at the exit of the combustor simulator.

For subsequent fillet optimizations, it was desired to apply inlet conditions as measured at the exit of the combustor simulator in the wind tunnel, which are believed to more accurately represent engine conditions. Utilizing measurements of temperature and total pressure taken above the slot at the inlet to the vane cascade, spanwise profiles of velocity and temperature were generated assuming a constant static pressure at the inlet plane. The generated profiles were then integrated to check that the passage mass flow was correct. The applied slot flow inlet boundary condition was one of constant velocity and temperature that yielded the correct percentage of total mass flow. Initial measurements of the thermal field at the exit of combustor simulator indicated a maximum temperature differential of approximately 11°C, which was deemed too small

for optimization purposes. Thus, the maximum temperature differential was increased to 35°C for the computations while nondimensionally the temperature profile was maintained the same (Case 2). For fillet experimental testing purposes, this development also led to investigation and modification of the wind tunnel thermal conditioning systems, ultimately resulting in an increase of the maximum achievable ΔT from 11 to 29°C. The resultant nondimensional profiles of total pressure and temperature for simulations including the backward-facing slot are presented in Figures 3.15 and 3.16, respectively. The experimental measurements, upon which the profiles are based, are also presented for comparison.

The computational results with the inclusion of the slot brought into question the advisability of a backward-facing slot design. The results of this investigation indicated significant ingestion of hot gas into the slot, even with an elliptical leading edge fillet in place. In an actual engine, such hot gas ingestion would result in increased thermal stress to the lip of the slot and possible premature part failure. The cause of ingestion is the relatively low momentum, low total pressure slot flow in comparison to the core flow above the slot as shown in Figure 3.15. The high total pressure fluid above the slot pushes down toward the endwall as it encounters the vane, easily displacing the lower momentum coolant exiting the slot. Similar results indicating hot gas ingestion were predicted in computations by Stitzel (2001), as shown in Figure 3.17. Figure 3.17 presents the velocity vectors in a plane extending directly upstream of the vane stagnation and clearly illustrates the action of the fluid above the slot as described above. Given these results, it was considered necessary to evaluate the effectiveness of the elliptical fillet in the absence of a slot. Thus, new inlet boundary conditions (Case 3) were developed to reflect elimination of the slot.

In developing the new boundary conditions (Case 3), the nondimensional profiles of total pressure and temperature as measured above the slot were now applied above the endwall. The resulting profiles are shown in Figures 3.18 and 3.19 along with experimental measurements for comparison. Due to thermal diffusion between the inlet of the solution domain and the inlet of the vane cascade, where experimental measurements were taken, a value of T_c was selected such that the computational nondimensional temperature profile at the cascade inlet closely matched experimental

results. The midspan and coolant temperatures, T_{ms} and T_c, for the applied temperature profile are presented in Table 3.2. Slight mismatch is shown between the total pressure profile applied in the computations and those measured; however, the peak is accurately modeled. The differences are attributable to modification of the combustor simulator to eliminate the backward-facing slot. Characterized by the magnitude of the total pressure peak, the pressure profile for this case will be referred to as the $\Delta p_{o,max} \approx 1$ profile. Without the backward-facing slot, the geometric restriction on fillet profile shape was also removed, enabling direct performance comparison between elliptical and linear fillets. A comparison between elliptical and linear fillet thermal performance was performed computationally, the results of which are presented in Chapter 5.

To computationally evaluate the robustness of the linear fillet ultimately tested, additional simulations were performed using an inlet total pressure profile with a more pronounced peak (Case 4). These simulations were computed upon completion of an experimental robustness study conducted in the wind tunnel vane cascade. The inlet conditions for the simulations were therefore based on the measured profile of total pressure as shown in Figure 3.20. The pressure profile for this case will be referred to as the $\Delta p_{o,max} \approx 2$ profile. In the experimental robustness study, the cascade inlet total pressure distribution was purposefully altered through adjustment of the coolant mass flow rate exiting each of the combustor simulator liner panels. Specifically, the coolant mass flow rates exiting the last two panels, panels 3 and 4, were increased to produce a larger near wall peak in total pressure. To compensate for the increased mass addition through these two panels, panels 1 and 2 of the combustor simulator were fully closed. A consequence of altering the inlet total pressure profile in this way was an associated change to the inlet thermal field. The temperature and total pressure field exiting the combustor simulator are both dictated by the distribution of coolant injection, and therefore the two are interdependent. A comparison of the experimentally measured temperature profiles for the two total pressure profiles considered is presented in Figure 3.21. The nondimensional temperature profiles for the $\Delta p_{o,max} \approx 2$ case indicate that the near-wall fluid is warmer than for the $\Delta p_{o,max} \approx 1$ case. Possible reasons for this increase in near-wall temperature are enhanced mixing of the coolant with the freestream fluid due

to increased momentum flux ratio and/or the lack of coolant exiting the first two panels of the combustor simulator.

Unlike the combustor simulator, CFD allows independent specification of the inlet total pressure and thermal fields. Therefore, to enable direct comparison of the computational results between the $\Delta p_{o,max} \approx 1$ and $\Delta p_{o,max} \approx 2$ cases, it was decided to maintain the same inlet temperature profile for the $\Delta p_{o,max} \approx 2$ case. The choice to maintain the same temperature profile however does not preclude comparison of the computations to experimental results. To compare the computational results to the experimental results, the computational value of T_c was adjusted to closely match the computed nondimensional temperature profile at the cascade inlet to the measured profile. Therefore, depending on the comparison being made, different values of T_c are assumed to match the nondimensional inlet temperature profile. The applied inlet nondimensional temperature profile used to match experimental measurements is shown in Figure 3.22, while the selected value of T_c is reported in Table 3.2.

3.6 Parametric Description of the Leading Edge Fillet

In any shape optimization problem, it is imperative that the specified geometric model be capable of assuming a great variety of shapes. The geometric model should allow for as much shape flexibility as possible with as few design parameters as possible. Obviously more shape flexibility is possible with a larger set of design parameters, but in terms of shape optimization, more design parameters translate into more computational time and expense. Therefore, one must strike a balance between geometric flexibility and the cost of such flexibility. It should also be acknowledged that specification of a geometric model effectively reduces the design space and directly affects determination of the optimum. Therefore, in any shape optimization effort, the determined optimum is dependent on the specified geometric model. While this fact may seem obvious, it is nontrivial and underscores the importance of geometric model selection.

To minimize the number of design parameters for the leading edge fillet, a geometric model of the fillet, including what are considered to be the most important design parameters, was developed. Although every imaginable fillet geometry cannot be described by the chosen set of parameters, it was hoped that most geometries could be

closely approximated using this mathematic description. As with the applied inlet boundary conditions, the geometric definition of the leading edge fillet also evolved throughout the design optimization process. For this reason, the fillet geometric definition as applied in the preliminary optimization effort will be presented first, followed by description of modifications made in subsequent optimization efforts.

The leading edge fillet geometry and associated design parameters utilized in the preliminary optimization are illustrated in Figure 3.23. A total of four parameters were selected to describe the shape of a fillet. The two parameters believed to be most important are the fillet maximum height, H_{max}, and the fillet maximum extent normal to the vane surface, D_{max}. The remaining two parameters, $s_{max,ps}$ and $s_{max,ss}$, specify how far the fillet extends along the vane pressure and suction surfaces. One of the restrictions of this parametric description is that the fillet maximum height and maximum extent are fixed at the vane dynamic stagnation point. Another restriction was placed on the fillet cross-sectional or surface profile. Given the success of the fillet investigated by Zess and Thole (1999), which featured a linear cross-sectional profile, a linear profile was also used in the preliminary optimization.

In addition to the leading edge fillet, a manufacturing fillet of height and extent D_{manuf}, was included in the geometric model around the trailing edge of the vane. The size of the manufacturing fillet was based on typical turbine design practices at Pratt & Whitney. Similar to the leading edge fillet, the manufacturing fillet profile was also specified as linear. The distance that the fillet extends normal to the vane surface, D(s), and the height of the fillet, H(s), are both expressed as functions of streamwise distance along the vane surface, s, in equations 3.5 through 3.8, where subscripts ps and ss indicate along the pressure and suction surfaces, respectively. By definition, s is positive along the suction surface and negative along the pressure surface.

$$D_{ps}(s) = \begin{cases} \frac{1}{2}(D_{max} - D_{manuf})\left[\cos\left(\pi\frac{s}{s_{max,ps}}\right)+1\right] + D_{manuf} & , 0 \geq s > s_{max,ps} \\ D_{manuf} & , s \leq s_{max,ps} \end{cases} \tag{3.5}$$

$$H_{ps}(s)=\begin{cases}\frac{1}{2}(H_{max}-D_{manuf})\left[\cos\left(\pi\frac{s}{s_{max,ps}}\right)+1\right]+D_{manuf} & ,\ 0\geq s>s_{max,ps}\\ D_{manuf} & ,\ s\leq s_{max,ps}\end{cases} \tag{3.6}$$

$$D_{ss}(s)=\begin{cases}\frac{1}{2}(D_{max}-D_{manuf})\left[\cos\left(\pi\frac{s}{s_{max,ss}}\right)+1\right]+D_{manuf} & ,\ 0\leq s<s_{max,ss}\\ D_{manuf} & ,\ s\geq s_{max,ss}\end{cases} \tag{3.7}$$

$$H_{ss}(s)=\begin{cases}\frac{1}{2}(H_{max}-D_{manuf})\left[\cos\left(\pi\frac{s}{s_{max,ss}}\right)+1\right]+D_{manuf} & ,\ 0\leq s<s_{max,ss}\\ D_{manuf} & ,\ s\geq s_{max,ss}\end{cases} \tag{3.8}$$

In subsequent optimization efforts, the fillet parametric description was modified. With the addition of the backward-facing slot, geometric interference issues between the slot and a fillet with a linear profile resulted in consideration of elliptical fillet designs. The choice of an elliptical fillet profile was attractive for several reasons. First, the elliptical shape allowed the fillet to extend further upstream without geometric interference with the slot. Second, elliptical fillets provided for smooth transitions between the fillet and vane and endwall surfaces, which was lacking with a linear design. Lastly, the choice of an elliptical profile precluded the need for additional design parameters. The fillet shape in a plane normal to the vane surface is expressed mathematically by Equation 3.9 and is illustrated in Figure 3.24.

$$\frac{(y-D)^2}{D^2}+\frac{(Z-H)^2}{H^2}=1 \tag{3.9}$$

Note that y is a local coordinate in the normal plane of interest, while H and D are the fillet height and extent, both of which are functions of the streamwise distance along the vane surface. With exception to shape modification, the mathematical expressions presented above for fillet height and extent normal to the vane surface remained valid.

The next and final modification made to the leading edge fillet definition was elimination of the constraint that maximum fillet height and extent occur at the vane dynamic stagnation. Additionally, this final modification removed the constraint that maximum fillet height and extent be collocated. Thus, two new design parameters, s_{Hmax} and s_{Dmax}, were introduced to specify the locations of maximum fillet height and extent, respectively. Figure 3.25 illustrates a fillet design with maximum fillet height and extent occurring along the pressure and suction surfaces, respectively. The mathematical expressions for fillet height and extent were recast as equations 3.10 through 3.13.

$$D_{ps}(s) = \begin{cases} \frac{1}{2}(D_{max} - D_{manuf})\left[\cos\left(\pi \frac{s_{Dmax} - s}{s_{Dmax} - s_{max,ps}}\right) + 1\right] + D_{manuf} & , s_{Dmax} \geq s > s_{max,ps} \\ D_{manuf} & , s \leq s_{max,ps} \end{cases} \tag{3.10}$$

$$H_{ps}(s) = \begin{cases} \frac{1}{2}(H_{max} - D_{manuf})\left[\cos\left(\pi \frac{s_{Hmax} - s}{s_{Hmax} - s_{max,ps}}\right) + 1\right] + D_{manuf} & , s_{Hmax} \geq s > s_{max,ps} \\ D_{manuf} & , s \leq s_{max,ps} \end{cases} \tag{3.11}$$

$$D_{ss}(s) = \begin{cases} \frac{1}{2}(D_{max} - D_{manuf})\left[\cos\left(\pi \frac{s - s_{Dmax}}{s_{max,ss} - s_{Dmax}}\right) + 1\right] + D_{manuf} & , s_{Dmax} \leq s < s_{max,ss} \\ D_{manuf} & , s \geq s_{max,ss} \end{cases} \tag{3.12}$$

$$H_{ss}(s)=\begin{cases}\dfrac{1}{2}\left(H_{max}-D_{manuf}\right)\left[\cos\left(\pi\dfrac{s-s_{Hmax}}{s_{max,ss}-s_{Hmax}}\right)+1\right]+D_{manuf} & , s_{Hmax}\le s<s_{max,ss}\\ D_{manuf} & , s\ge s_{max,ss}\end{cases} \tag{3.13}$$

The subscripts ps and ss were retained to indicate to which side of the maximum fillet height and extent locations the equations apply. Thus, ss denotes applicability toward the suction side of the maximum location, even though the maximum might be located along the pressure side. With elimination of the backward-facing slot, both linear and elliptical fillets were considered using this modified geometric definition.

3.7 Objective Function Definition and Evaluation

Prior to discussing the selection of an objective function for this investigation, the mathematical formulation of the optimization problem will be presented. In general, any nonlinear constrained optimization problem can be expressed mathematically by a similar set of equations. The goal of the optimization process is to minimize or maximize the defined objective function, F, which can be expressed as a function of a design variable vector, **X**.

$$\text{Minimize/Maximize: } F(\mathbf{X}) \tag{3.14}$$

As an example, the design variable vector for the preliminary optimization effort as defined in the previous section can be expressed mathematically as follows:

$$\mathbf{X}=\begin{Bmatrix}D_{max}\\ H_{max}\\ s_{max,ps}\\ s_{max,ss}\end{Bmatrix} \tag{3.15}$$

An optimization problem is usually subject to additional constraints, which can be grouped into the following three main categories: inequality constraints, equality

constraints, and side constraints. These various constraint types are expressed mathematically in Equations 3.16 through 3.18.

$$\text{Inequality constraints: } g_j(\mathbf{X}) \le 0 \qquad j = 1, m \tag{3.16}$$

$$\text{Equality constraints: } h_k(\mathbf{X}) = 0 \qquad k = 1, l \tag{3.17}$$

$$\text{Side constraints: } X_i^l \le X_i \le X_i^u \qquad i = 1, n(\#\text{ design variables}) \tag{3.18}$$

In this investigation, no inequality or equality constraints were imposed. These constraints typically specify additional design requirements that must be met in the optimization process. For example, an upper limit on acceptable pressure drop may be imposed on the design of a fluid coupler, thereby restricting the optimum design from regions of the design space that violate this limit. Equality constraints can be either explicit or implicit functions in **X**. If equality constraints are explicit in **X**, they can often be used to reduce the number of design variables in the optimization process. Side constraints define the extent of the design space by placing a lower bound, X_i^l, and an upper bound, X_i^u, on the value of each design variable. The side constraints applied in the preliminary optimization (Case 1) are as follows.

$$0.084 \le D_{max}/C \le 0.227 \tag{3.19}$$

$$0.042 \le H_{max}/C \le 0.227$$

$$0.100 \le s_{max,ps}/s_{total,ps} \le 0.970$$

$$0.085 \le s_{max,ss}/s_{total,ss} \le 0.440$$

The upper constraint on maximum fillet extent was set to eliminate interference between fillets applied to adjacent vanes. In the event that adjacent fillets would overlap in the vane passage, GAMBIT would be unable to create the geometry and mesh. The upper constraint on maximum fillet height was set identical to that for the extent, limiting the

fillet height to approximately 25% of the vane span. These constraints also ensured that the fillet size did not become impractical from a manufacturing standpoint. The constraints on $s_{max,ps}$ and $s_{max,ss}$ were set such that the gage point of the vane passage remained unchanged. The principal ramification of maintaining the gage point was that the fillet could not extend beyond the passage throat along the suction surface. Thus, the region of uncovered turning is characterized by a manufacturing fillet. Similar side constraints were applied in the optimization of an elliptical fillet with backward-facing slot coolant injection (Case 2a), as given in equation 3.20.

$$0.084 \le D_{max}/C \le 0.160 \tag{3.20}$$
$$0.084 \le H_{max}/C \le 0.160$$
$$0.189 \le s_{max,ps}/s_{total,ps} \le 0.970$$
$$0.130 \le s_{max,ss}/s_{total,ss} \le 0.437$$

The most notable difference from the constraints applied in the preliminary optimization is a reduction in the maximum allowable fillet height and extent. These reductions were necessary to preclude interference between the fillet and backward-facing slot. Finally, side constraints were applied to s_{Dmax} and s_{Hmax} for investigation of the impact of maximum fillet height and extent locations on fillet performance (Case 2b).

$$-0.337 \le s_{Dmax}/C \le 0.231 \tag{3.21}$$
$$-0.337 \le s_{Hmax}/C \le 0.231$$

A summary of the design variables and constraints for the various optimization efforts is given in Table 3.3.

The goal of this investigation was to minimize the temperatures experienced by the endwall and vane surfaces through application of a leading edge fillet. Since these surfaces were modeled as adiabatic, definition of an objective function appeared to be straightforward. At the start of this optimization effort, the area-weighted average

surface temperature, expressed mathematically by Equation 3.22, was selected as the objective function.

$$F_1(\mathbf{X}) = \frac{1}{A}\iint_A T_{aw}\,dA \tag{3.22}$$

However, upon consideration of possible local hot spots, it was decided that this also had to be factored into the objective function. This was accomplished by utilizing the area-weighted average of the square of the surface temperature given in Equation 3.23.

$$F_2(\mathbf{X}) = \frac{1}{A}\iint_A T_{aw}^2\,dA \tag{3.23}$$

This choice effectively takes into account local hot spots in determination of design performance. In the preliminary optimization, both objective functions were recorded and were found to yield the same optimum fillet geometry. For this reason, the original objective function, $F_1(X)$, was utilized in subsequent optimization efforts. To determine fillet thermal performance relative to a vane with only a manufacturing fillet, the objective functions were normalized by the calculated results for the baseline geometry, as expressed in equations 3.24 and 3.25.

$$F_{1,norm}(\mathbf{X}) = \frac{\frac{1}{A}\iint_A T_{aw}\,dA}{\left.\frac{1}{A}\iint_A T_{aw}\,dA\right|_{Baseline}} \tag{3.24}$$

$$F_{2,norm}(\mathbf{X}) = \frac{\frac{1}{A}\iint_A T_{aw}^2\,dA}{\left.\frac{1}{A}\iint_A T_{aw}^2\,dA\right|_{Baseline}} \tag{3.25}$$

The results of all optimization efforts are presented in Chapter 5 of this document.

3.8 Thermal Field and Secondary Flow Analysis

To visualize the impact of a leading edge fillet on the flow, the thermal and secondary flow fields were examined in select flow planes throughout the vane passage. In addition, the resulting distributions of adiabatic wall temperature on the endwall, fillet, and vane surfaces were also examined. This section provides the details of the thermal and secondary flow analyses, while the computational and experimental results of these analyses are presented in Chapters 5 and 6, respectively.

To quantify the thermal performance and benefit of fillet application, baseline unfilleted simulations and experiments were conducted to provide a basis for comparison. Therefore, the thermal benefit presented by a fillet is quantified through comparison to the corresponding baseline results. Comparisons were made on a number of different levels, ranging from qualitative to quantitative. This section presents the various means of comparison utilized in this investigation. Not all methods of comparison were applied to both computational and experimental results mainly due to limited experimental data. As the various methods of comparison are presented, limitations to their application will be discussed.

For qualitative visual comparisons, contour plots of endwall adiabatic effectiveness, as defined in equation 3.26, were generated for both baseline and filleted vane results.

$$\eta = \frac{T_{ms} - T_{aw}}{T_{ms} - T_c} \tag{3.26}$$

The midspan and coolant temperatures, T_{ms} and T_c, are defined as previously described in section 3.5, while T_{aw} is the adiabatic wall temperature. The term endwall is used rather loosely in this instance, as it is extended to include the non-planar fillet surface in addition to the planar endwall surface upon which the vane rests. In generating the contour plots, the temperature results on all fillet surfaces were projected onto the endwall. Thus, what is actually a three-dimensional result was projected to two-dimensions for the sake of visual comparison. This leads to a very important distinction

that needs to be made when comparing baseline effectiveness levels with those of a fillet. While the contours for the baseline case represent the temperature distribution on a flat endwall, those for the filleted case represent the temperature distribution on the endwall and fillet, which extends up the vane span toward hotter mainstream flow temperatures. Given this geometric difference, a fair comparison is not truly possible. Despite this fact, this method of comparison does offer insight into where thermal benefit is being realized, though it provides no rigorous quantification of the observed benefit. Additionally, this means of comparison is equally applicable to both computational and experimental results.

To quantify the thermal benefit observed through comparison of baseline and filleted contour plots of adiabatic wall temperature, a MATLAB code was written to calculate lateral average adiabatic effectiveness at various axial locations throughout the vane passage. The code calculates the lateral average at each given axial location through numerical integration of the adiabatic effectiveness distribution and division by the cross-passage distance, expressed mathematically by equation 3.27.

$$\bar{\eta} = \frac{\int_{ss}^{ps} \eta(\xi)\, d\xi}{\int_{ss}^{ps} d\xi} \tag{3.27}$$

The limits of integration, ss and ps, indicate integration across the passage from suction surface to pressure surface, while $d\xi$ represents an infinitesimal cross-passage length. As in the generation of the contour plots discussed above, the data supplied to the MATLAB code was projected onto the endwall. Therefore, the lateral average effectiveness results also do not represent a one to one comparison in the strictest sense; however, they do provide a reasonable quantitative means of comparison. The MATLAB code use to perform the lateral averaging is included in Appendix C.

To further condense the lateral average effectiveness results, the calculated values were used to calculate area-weighted average adiabatic effectiveness. This was done by weighting the lateral average effectiveness results by their corresponding cross-passage lengths and dividing by the cumulative length, as expressed in equation 3.28.

$$\bar{\bar{\eta}} = \frac{\sum_{i=1}^{n} \bar{\eta}_i l_i}{\sum_{i=1}^{n} l_i} \tag{3.28}$$

Calculated values of area-weighted average effectiveness enabled a single integrated value comparison between baseline and filleted wall temperature distributions.

Thus far, the discussed means of quantifying fillet thermal benefit have focused exclusively on the endwall and fillet surfaces for which experimental data are available. Another method for quantifying thermal benefit, applied only to the computational results, is to isolate and analyze each flow surface separately. As an example, the manufacturing fillet in the baseline case is considered equivalent to the design fillet in the filleted case, even though the two may be vastly different in surface area. To account for the differences in area, the area-weighted average adiabatic wall temperature was calculated and compared for each geometric feature. The thermal benefit realized by each surface was subsequently expressed as a percentage of the maximum heat transfer driving potential observed in the flow using equation 3.29.

$$TB[\%] = \frac{\bar{T}_{aw,baseline} - \bar{T}_{aw,fillet}}{T_{ms} - T_c} \times 100 \tag{3.29}$$

Another means of evaluating the thermal benefit is to calculate the percentage increase in area-weighted average adiabatic effectiveness, as expressed by equation 3.30.

$$TB_{\eta}[\%] = \frac{\bar{\bar{\eta}}_{fillet} - \bar{\bar{\eta}}_{baseline}}{\bar{\bar{\eta}}_{baseline}} \times 100 \tag{3.30}$$

Though equation 3.30 may appear similar to equation 3.29, the results of the two equations are not the same due to a difference in the denominator. Upon substitution and simplification, equation 3.30 can be expressed as follows.

$$TB_{\eta}[\%] = \frac{\overline{T}_{aw,baseline} - \overline{T}_{aw,fillet}}{T_{ms} - \overline{T}_{aw,baseline}} \times 100 \tag{3.31}$$

Instead of the coolant temperature, the area-weighted average adiabatic wall temperature for the baseline appears in the denominator. It is important to note that while the coolant temperature is constant in the definition of TB, the baseline average adiabatic wall temperature in TB_{η} varies from surface to surface. Due to the lack of vane surface temperature measurements, these methods of evaluation were only applied to the computational results. Results of analyses of this kind are presented in tabular form in Chapter 5.

To further resolve the distribution of thermal benefit on the various flow surfaces, another method of comparison was developed. The concept behind the method is to divide the vane and fillet into equal-height spanwise segments, to calculate the area-weighted average adiabatic wall temperature of each segment, and finally to compare the results for the baseline and filleted cases. This method was successfully applied to computational results, dividing the vane and attached fillet into segments of 5% of the vane span. The spanwise distributions of area-weighted average adiabatic wall temperature were then visualized through bar chart comparison of the baseline and filleted vane results, as is presented in Chapter 5. Additionally, the thermal benefit realized by each spanwise segment was calculated using equation 3.29, and the results were plotted as a function of spanwise location.

In addition to comparison of the temperature distributions on the endwall, fillet, and vane surfaces, the impact of a leading edge fillet on the thermal field in select flow planes was also considered. To visualize the thermal field within the turbine vane passage, several analysis planes oriented perpendicular to the vane surface were defined as shown in Figure 3.26. The analysis plane naming convention employed was to designate pressure side planes with the prefix PS, suction side planes with the prefix SS and the stagnation plane by SP. For qualitative visual comparison of thermal fields, contour plots of nondimensional flow temperature, as defined by equation 3.32, were generated for both baseline and filleted vane results.

$$\theta = \frac{T_{ms} - T}{T_{ms} - T_c} \tag{3.32}$$

While computational results could be extracted for any of the analysis planes illustrated in Figure 3.26, experimental thermal field measurements were limited to the SS2 plane. The SS2 plane was selected for measurement based on computational results, which showed it to be a good indicator of fillet performance.

To visualize the secondary flows within the turbine vane passage, secondary flow velocities were calculated in the same analysis planes described above and shown in Figure 3.26. Planes normal to the vane surface were chosen to better highlight the secondary flows. The process of calculating the secondary flow velocities, developed by Hermanson (1999), has numerous steps that will be described in this section. To help the reader visualize the calculations, the process is illustrated in Figure 3.27.

The first step in calculating the secondary flow field is to transform the global coordinates and velocities at each point in the analysis plane into the local coordinate frame of the plane. This transformation is expressed mathematically by the following equations:

$$x = (X - X_o)\cos\beta + (Y - Y_o)\sin\beta \tag{3.33}$$

$$y = -(X - X_o)\sin\beta + (Y - Y_o)\cos\beta \tag{3.34}$$

$$z = Z \tag{3.35}$$

where X_o and Y_o are the global coordinates of the intersection point of the analysis plane and vane surface and β is the angular rotation of the analysis plane relative to the global coordinate system. Since the local coordinate system is aligned with the analysis plane, all points in the plane have an x coordinate value of zero by definition. In addition, flow simulation results were extracted at uniformly distributed points in the analysis plane, yielding discrete values of y and z. Thus, the spacing of points in the *y* and *z* directions are equivalent($\Delta y = \Delta z$), and each point in the plane can be uniquely described by the y and z coordinates. The global velocities (U, V, W) in the plane of interest are then transformed into local coordinate velocities (u, v, w) using equations 3.36 through 3.38.

$$u = U\cos\beta + V\sin\beta \tag{3.36}$$

$$v = -U\sin\beta + V\cos\beta \tag{3.37}$$

$$w = W \tag{3.38}$$

Next, the midspan flow angle for each pitch location(y location) in the analysis plane is calculated using equation 3.39.

$$\Psi_{ms}(y) = \tan^{-1}\left(\frac{v_{ms}}{u_{ms}}\right) \tag{3.39}$$

The resulting midspan flow angle is therefore relative to the x-axis of the local coordinate frame. Finally, the velocity components (u, v, w) for all points in the plane are transformed into streamwise and normal components (V_s, V_n, V_z) with the streamwise direction being defined by the midspan flow angle. This transformation is expressed by the following equations.

$$V_s = u\cos\Psi_{ms} + v\sin\Psi_{ms} \tag{3.40}$$

$$V_n = -u\sin\Psi_{ms} + v\cos\Psi_{ms} \tag{3.41}$$

$$V_z = w \tag{3.42}$$

To visualize the secondary flows, vector plots of the velocity components normal to the streamwise direction (V_n and V_z) can be constructed. Plots of this type are instrumental in illustrating the secondary flow patterns, and are used as a means of comparison between filleted and unfilleted vane passage flows. It should be noted that these secondary flow velocity components, though plotted as if in the analysis plane, differ from the in-plane components. This is due to the fact that the midspan flow angle is not necessarily perpendicular to the analysis plane. Nonetheless, vector plots of this sort are extremely useful.

This chapter has presented the details of the computational and optimization approach taken in this investigation, as well as the various methods of analysis utilized to

quantify the thermal benefit of a leading edge fillet. To ensure the most accurate computational results, the turbulence model selected for closure of the Reynolds-averaged Navier-Stokes and energy equation, and the choice of near-wall treatment were based on past success in predicting secondary flows documented by Hermanson and Thole (1999). More realistic turbine inlet boundary conditions were applied in the computations and optimization, developed from experimental measurements taken at the exit of a combustor simulator. The geometric models used to describe leading edge fillet shape were developed to provide as much shape flexibility as possible with as few design parameters as possible. Due to geometric constraints imposed by the upstream combustor simulator, the fillet model and associated design parameters evolved throughout the design optimization process and led to the investigation of fillet profile shape. The selection of an objective function for the optimization process was driven by the desire to quantify the thermal benefit of a leading edge fillet. In the next chapter, details of the experimental phase of this investigation are presented.

Table 3.1 Operating parameters of the turbine vane at engine conditions and wind tunnel testing conditions.

	Engine Conditions	Model Conditions
True Chord, C (cm)	6.6	59.4
Axial Chord, C_{axial} (cm)	3.2	28.8
Aspect Ratio, C/S	1.08	1.08
Solidity Ratio, C/P	1.30	1.30
Pressure surface length, $s_{total,ps}$ (cm)	5.9	53.0
Suction surface length, $s_{total,ss}$ (cm)	8.5	76.7
Inlet Mach Number	0.12	0.02
Exit Mach Number	0.90	~0.1
Inlet Reynolds Number, $Re_{inlet}=\rho U_{inlet}C/\mu$	2.3×10^5	2.3×10^5
Exit Reynolds Number, $Re_{exit}=\rho U_{exit}C/\mu$	1.2×10^6	1.1×10^6
Stagnation Temperature (K)	1666	295
Stagnation Pressure (Pa)	10.3×10^5	~1 atm
Inlet Flow Angle (°)	0	0
Exit Flow Angle (°)	78	78
Manufacturing Fillet Extent, D_{manuf} (cm)	0.13	1.1

Table 3.2 Summary of computational inlet boundary conditions.

Case	Description	T_{ms} [K]	T_{min} [K]	T_c [K]	U_{slot} [m/s]	Figures
1	Turbulent Boundary Layer	340.5	214.5	214.5	N/A	3.9 – 3.13
2	Windtunnel Conditions w/ Slot, $\Delta p_{o,max} \approx 1$	313.2	278.2	278.2	1.295	3.15, 3.16
3	Windtunnel Conditions w/o Slot, $\Delta p_{o,max} \approx 1$	316.2	290.2	276.2	N/A	3.18, 3.19
4	Windtunnel Conditions w/o Slot, $\Delta p_{o,max} \approx 2$	316.2	290.2	270.2	N/A	3.20, 3.22

Table 3.3 Summary of the design variables and constraints for the various cases.

Case	Description	Design Variables	Design Constraints	Method
1	Linear Fillet	D_{max} H_{max} $s_{max,ps}$ $s_{max,ss}$	$0.084 \le D_{max}/C \le 0.227$ $0.042 \le H_{max}/C \le 0.227$ $0.100 \le s_{max,ps}/s_{total,ps} \le 0.970$ $0.085 \le s_{max,ss}/s_{total,ss} \le 0.440$	Simulated Annealing
2a	Elliptical Fillet	D_{max} H_{max} $s_{max,ps}$ $s_{max,ss}$	$0.084 \le D_{max}/C \le 0.160$ $0.084 \le H_{max}/C \le 0.160$ $0.189 \le s_{max,ps}/s_{total,ps} \le 0.970$ $0.130 \le s_{max,ss}/s_{total,ss} \le 0.437$	DOE
2b	Off-Stagnation Elliptical Fillet	s_{Dmax} s_{Hmax}	$D_{max}/C = 0.160$ $H_{max}/C = 0.160$ $s_{max,ps}/s_{total,ps} = 0.970$ $s_{max,ss}/s_{total,ss} = 0.437$ $-0.337 \le s_{Dmax}/C \le 0.231$ $-0.337 \le s_{Hmax}/C \le 0.231$	DOE
3	Linear vs. Elliptical Fillet	Fillet Profile Shape	$D_{max}/C = 0.160$ $H_{max}/C = 0.160$ $s_{max,ps}/s_{total,ps} = 0.970$ $s_{max,ss}/s_{total,ss} = 0.437$ $s_{Dmax}/C = 0.058$ $s_{Hmax}/C = 0.115$	N/A
4	Linear Fillet Robustness	N/A	$D_{max}/C = 0.160$ $H_{max}/C = 0.160$ $s_{max,ps}/s_{total,ps} = 0.970$ $s_{max,ss}/s_{total,ss} = 0.437$ $s_{Dmax}/C = 0.058$ $s_{Hmax}/C = 0.115$	N/A

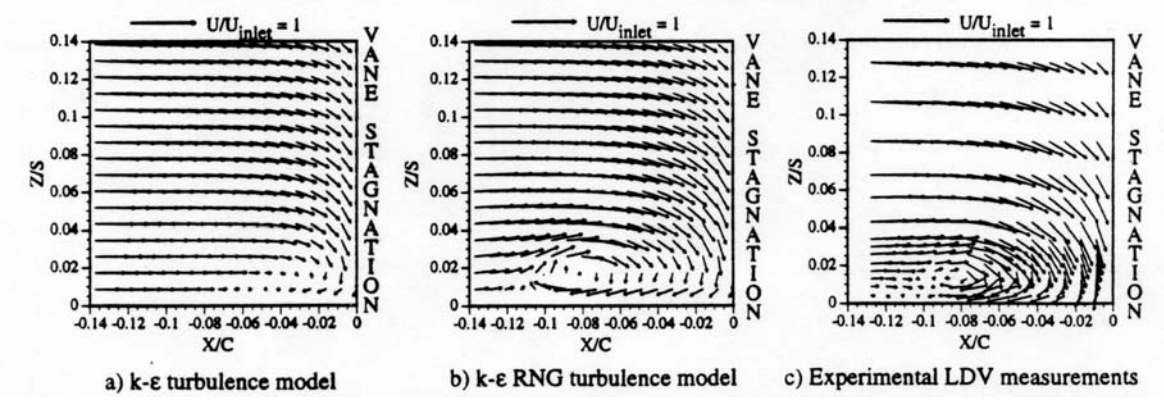

Figure 3.1 Benchmarking of turbulence models with experimental LDV measurements in the leading edge stagnation plane performed by Hermanson (1999).

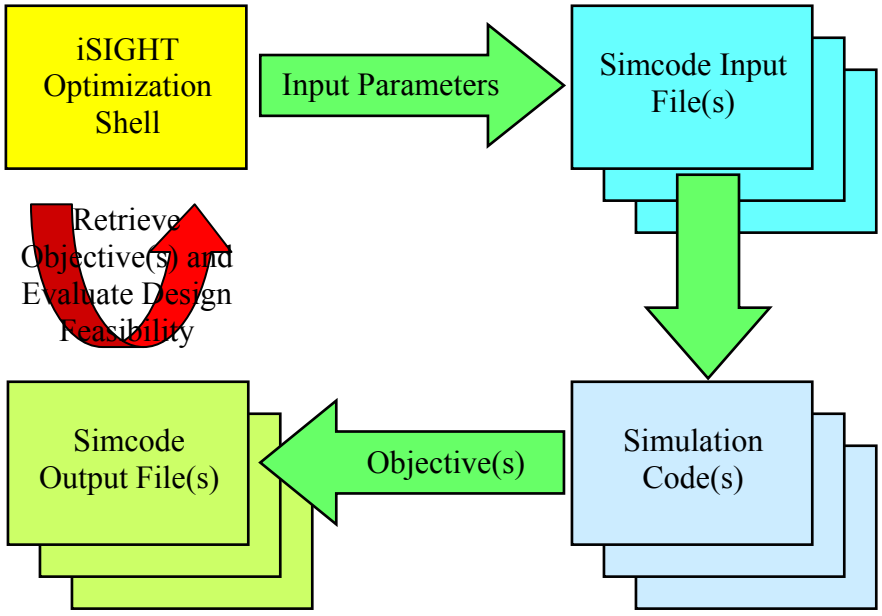

Figure 3.2 Automation of the design-evaluate-redesign cycle using iSIGHT.

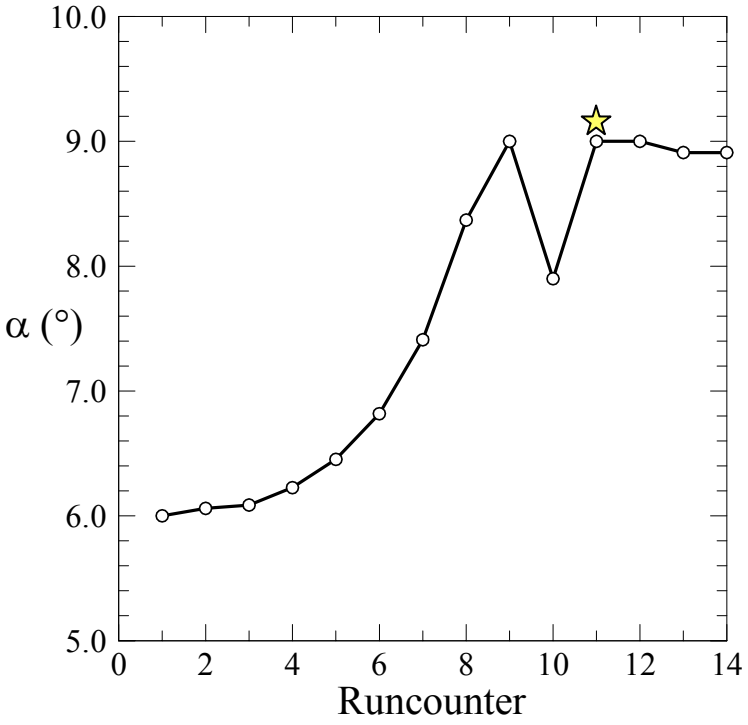

Figure 3.3 Convergence history for the NACA0012 proof-of-concept optimization with the optimum indicated by a star.

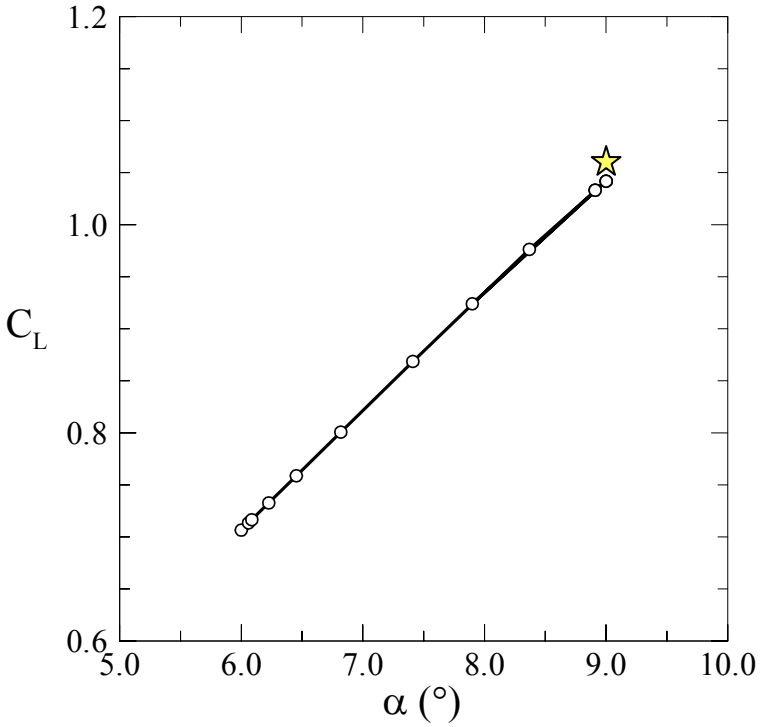

Figure 3.4 Coefficient of lift versus angle of attack for the NACA0012 proof-of-concept optimization.

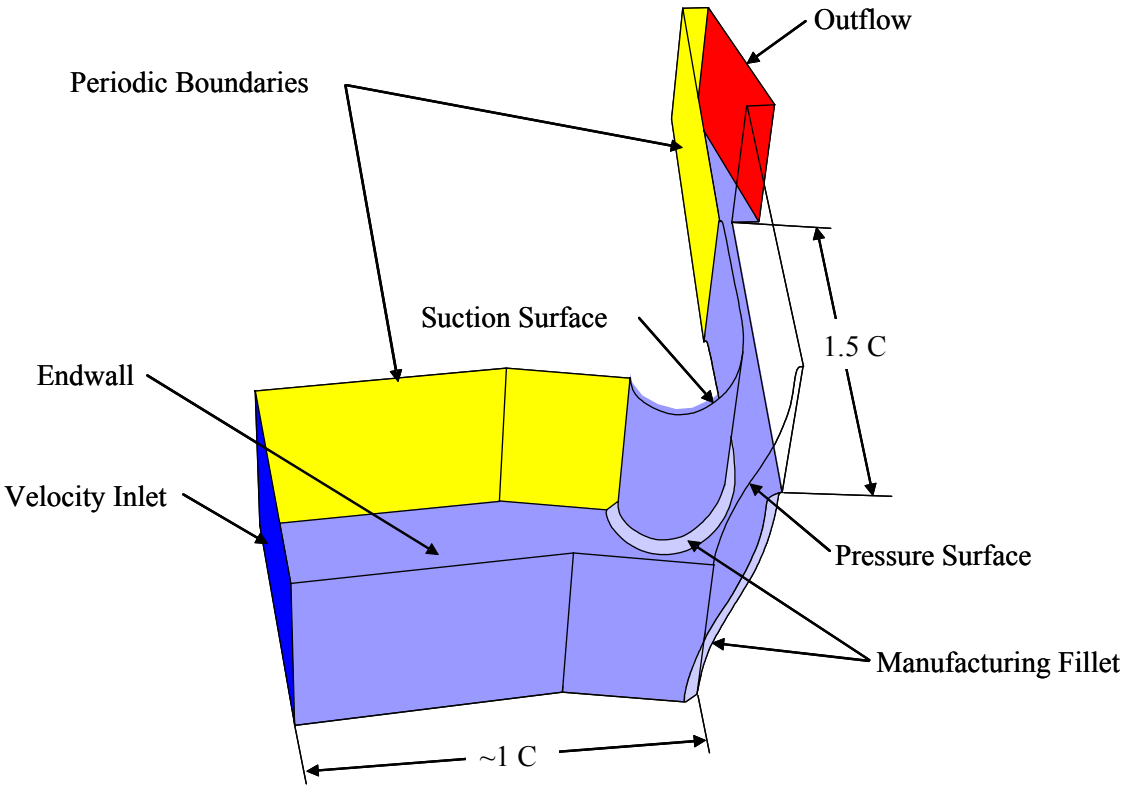

Figure 3.5 Illustration of the baseline computational solution domain for the preliminary optimization.

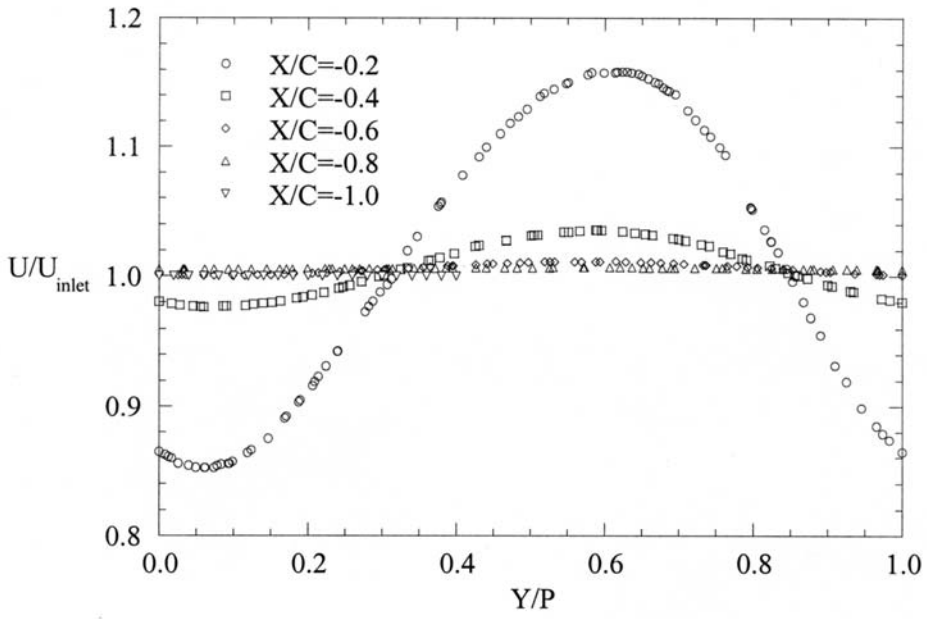

Figure 3.6 Predicted profiles of streamwise velocity at various locations upstream of the vane cascade by Hermanson(1999).

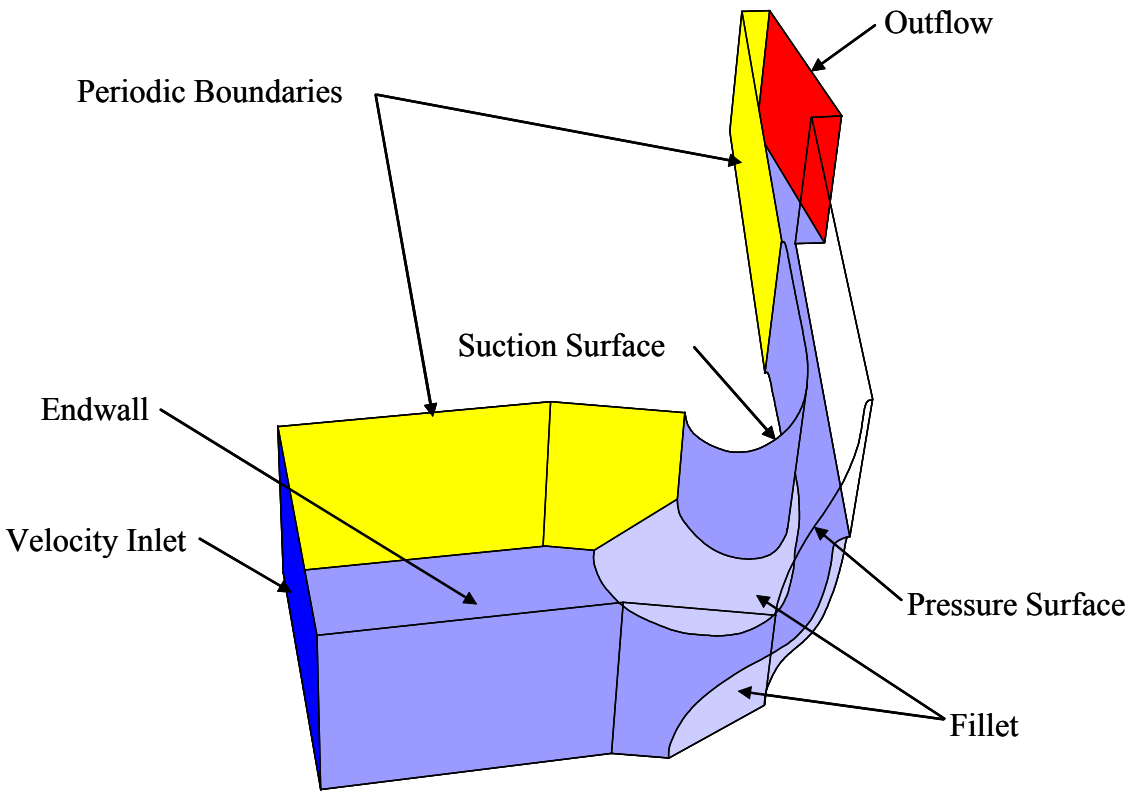

Figure 3.7 Illustration of representative filleted computational solution domain for the preliminary optimization.

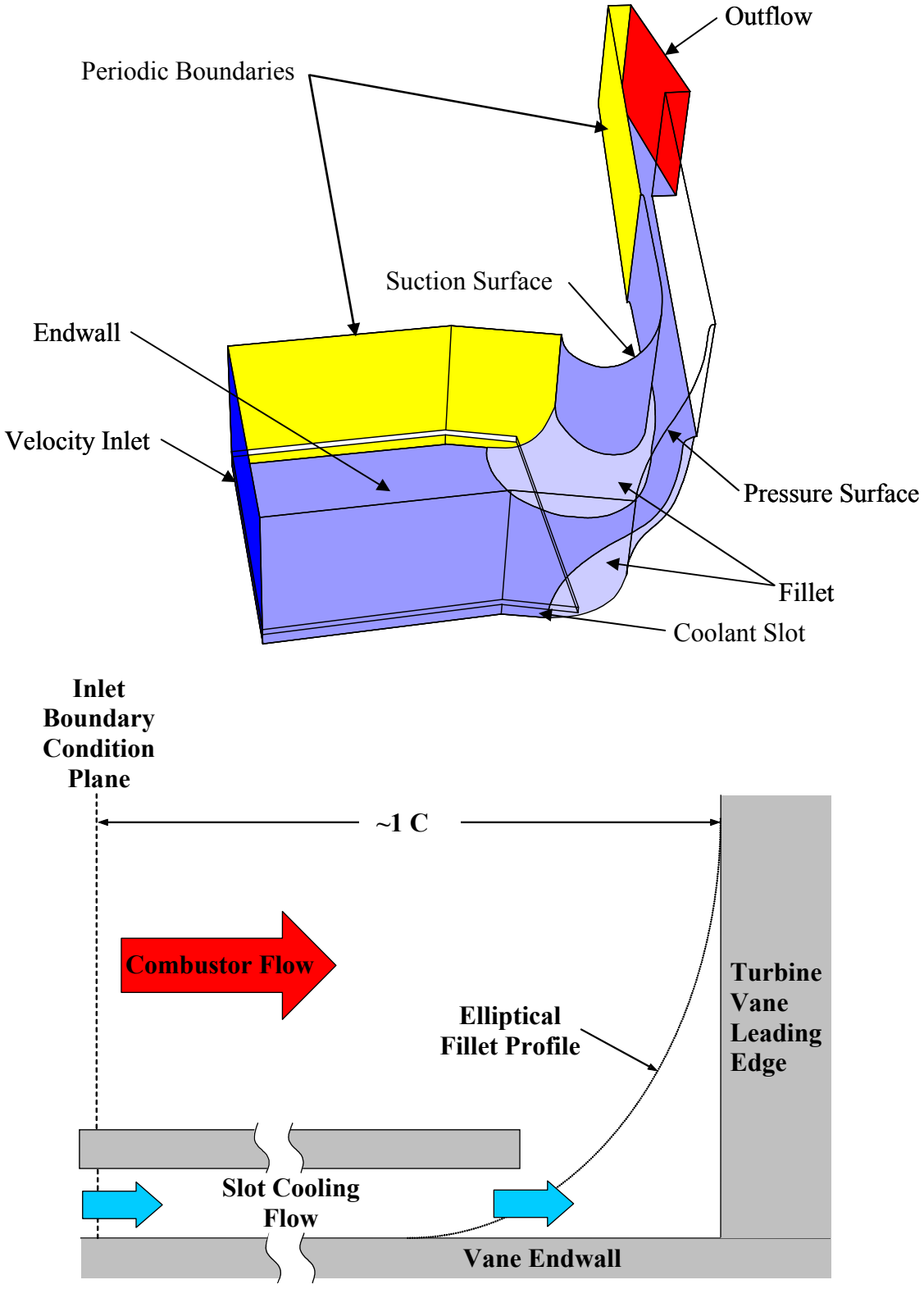

Figure 3.8 Illustration of the computational solution domain with a backward-facing cooling slot and cross-sectional detail in the vane leading edge region.

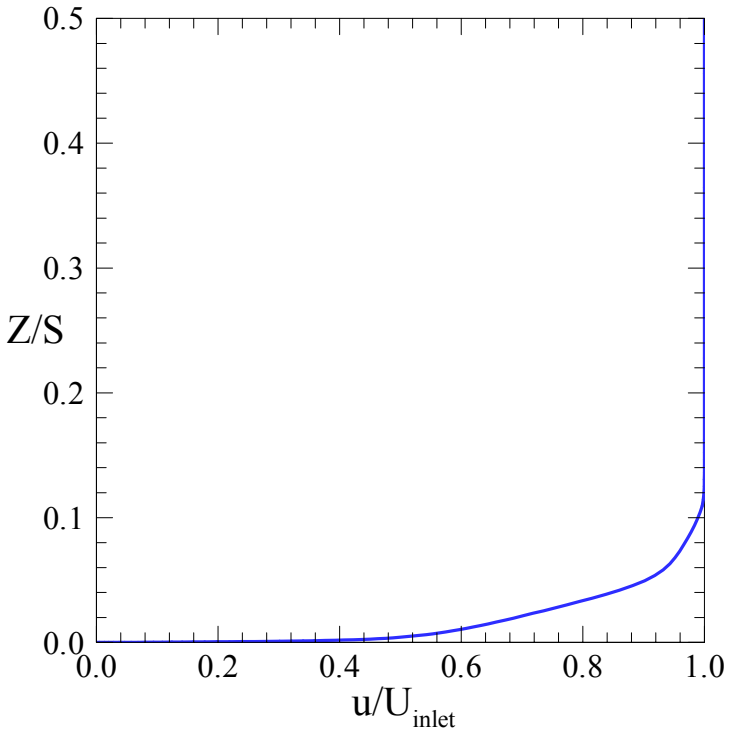

Figure 3.9 Inlet velocity profile for preliminary fillet optimization (Case 1).

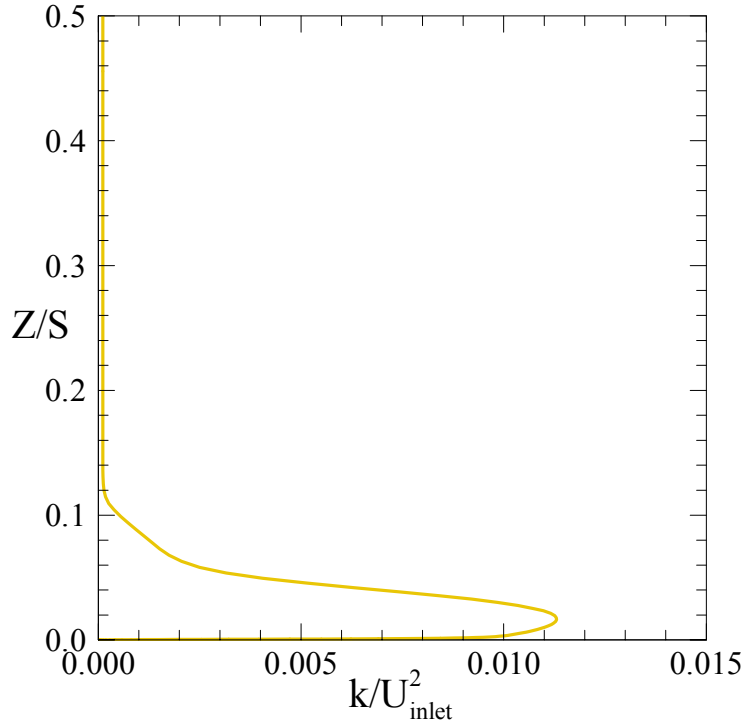

Figure 3.10 Inlet profile of turbulent kinetic energy for the preliminary fillet optimization (Case 1).

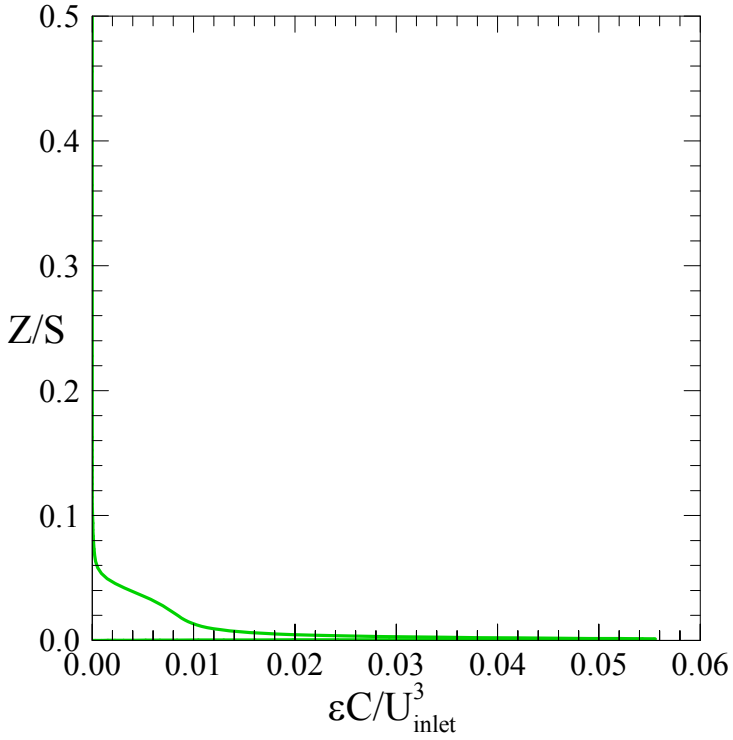

Figure 3.11 Inlet profile of turbulence dissipation rate for the preliminary fillet optimization (Case 1).

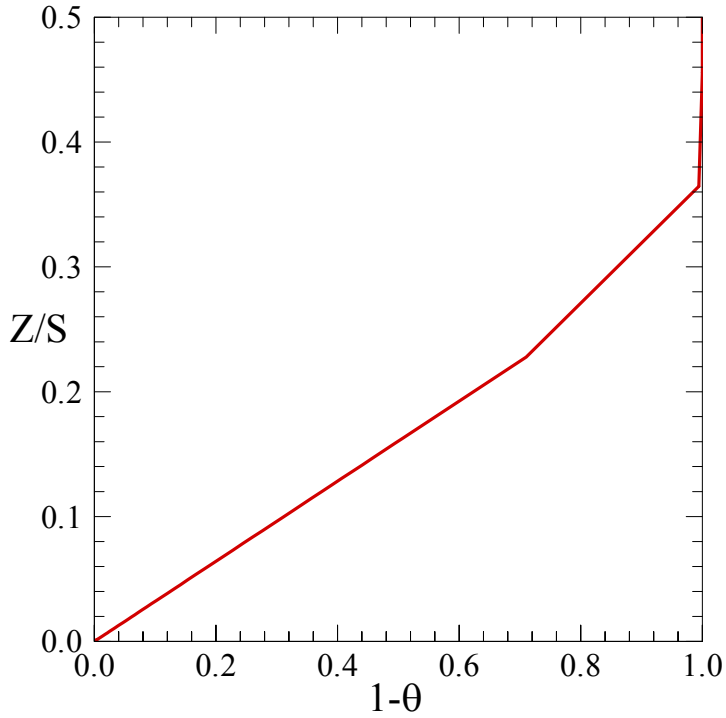

Figure 3.12 Inlet profile of flow temperature for the preliminary fillet optimization (Case 1).

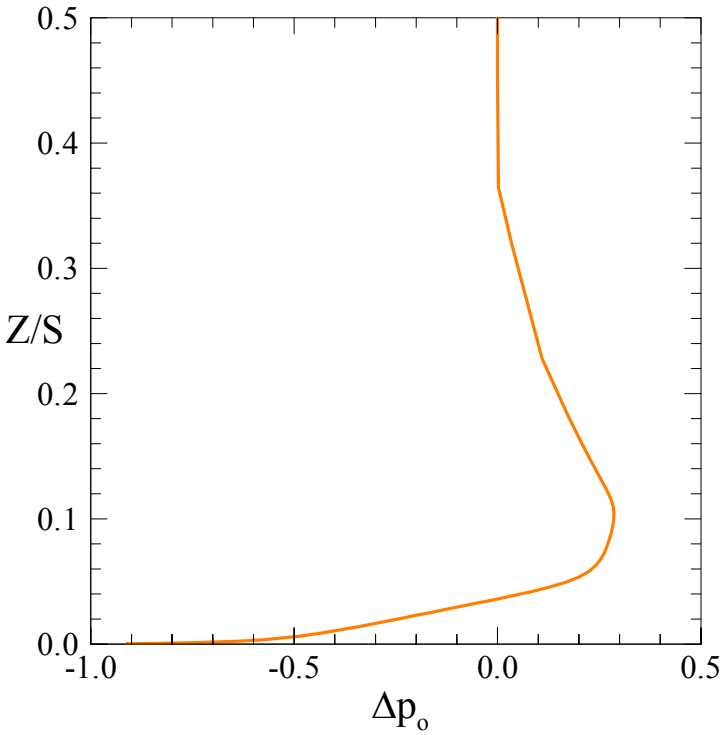

Figure 3.13 Inlet profile of total pressure for the preliminary fillet optimization (Case 1).

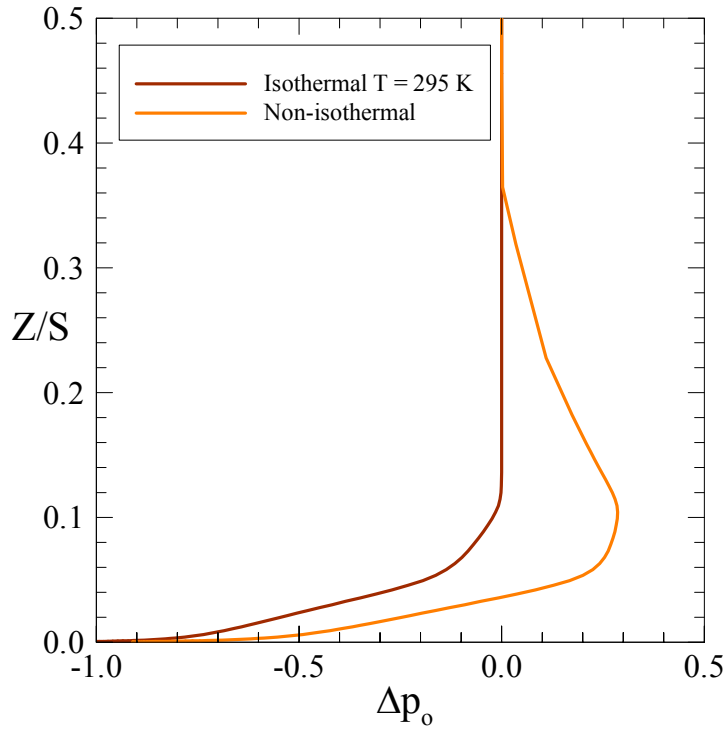

Figure 3.14 Comparison of the total pressure profiles resulting from non-isothermal and isothermal inlet conditions (Case 1).

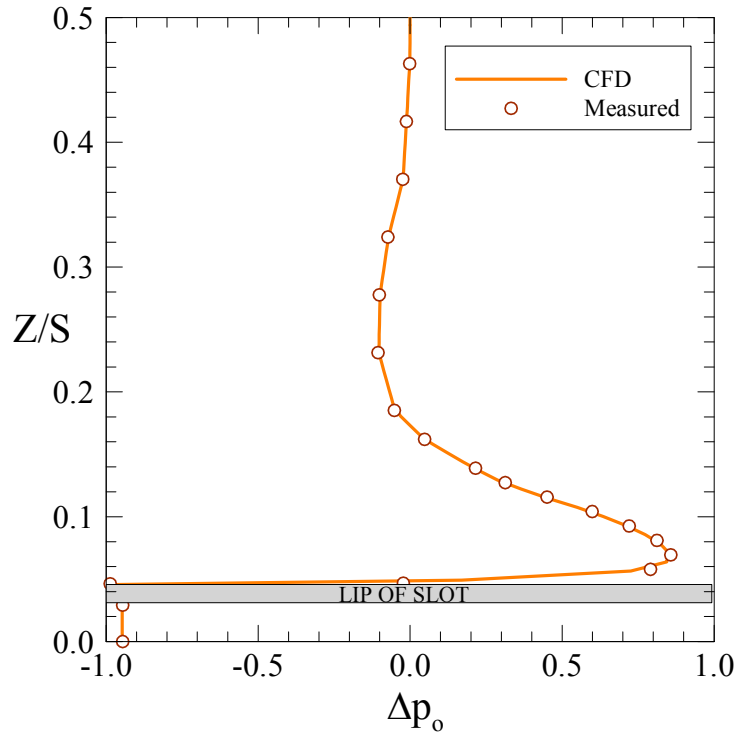

Figure 3.15 Inlet spanwise profile of normalized total pressure applied for computations with slot coolant injection compared to experimental measurements (Case 2).

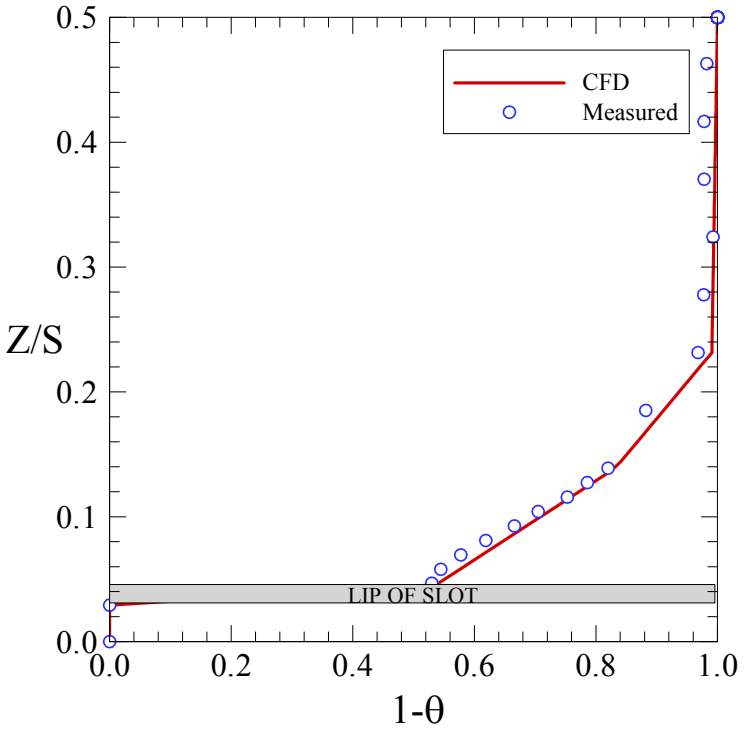

Figure 3.16 Inlet spanwise temperature profile applied for computations with slot coolant injection compared to experimental measurements (Case 2).

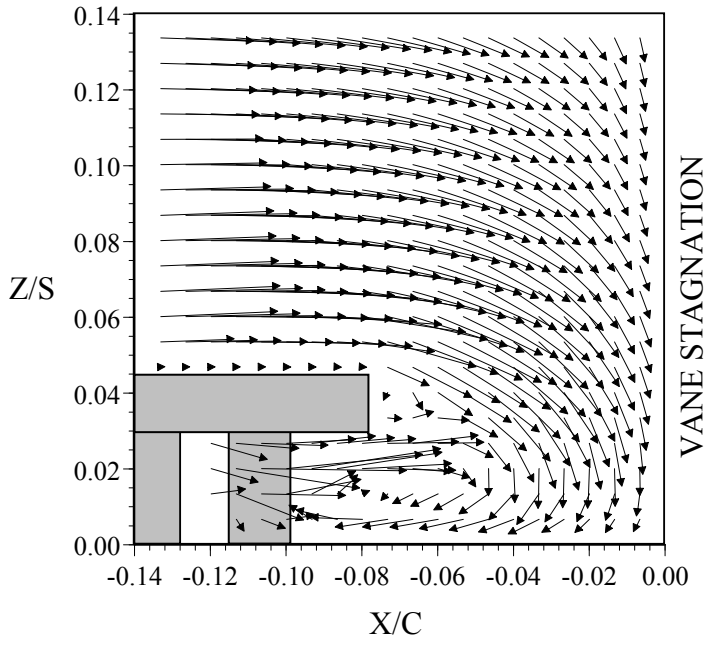

Figure 3.17 Computational results of Stitzel (2001) indicated hot gas ingestion into the backward-facing slot.

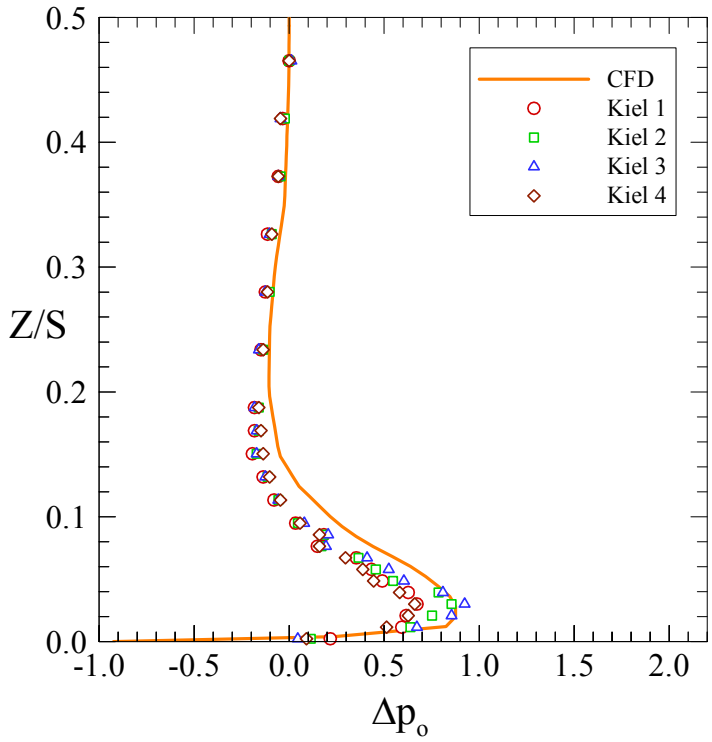

Figure 3.18 Inlet spanwise profile of normalized total pressure applied for computations without the backward-facing slot compared to experimental measurements (Case 3).

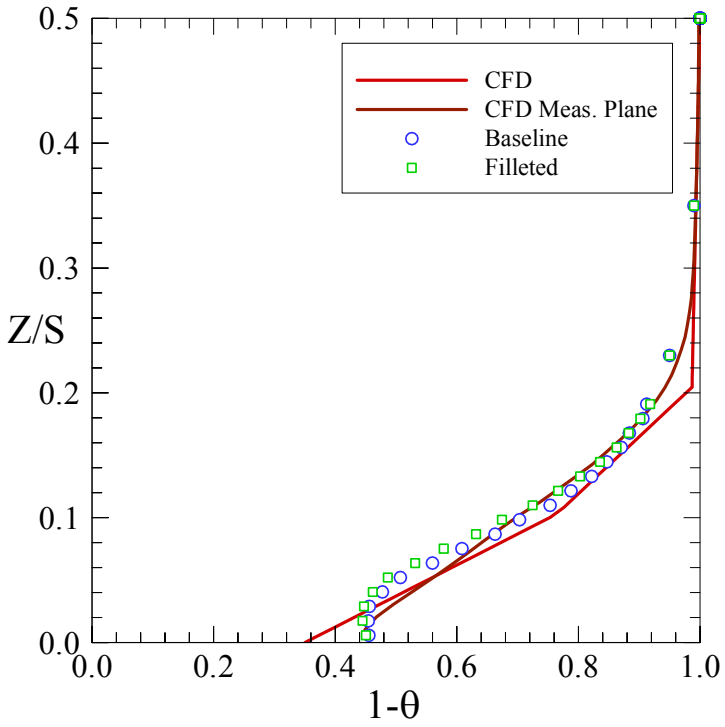

Figure 3.19 Inlet spanwise temperature profile applied for computations without the backward-facing slot compared to experimental measurements (Case 3).

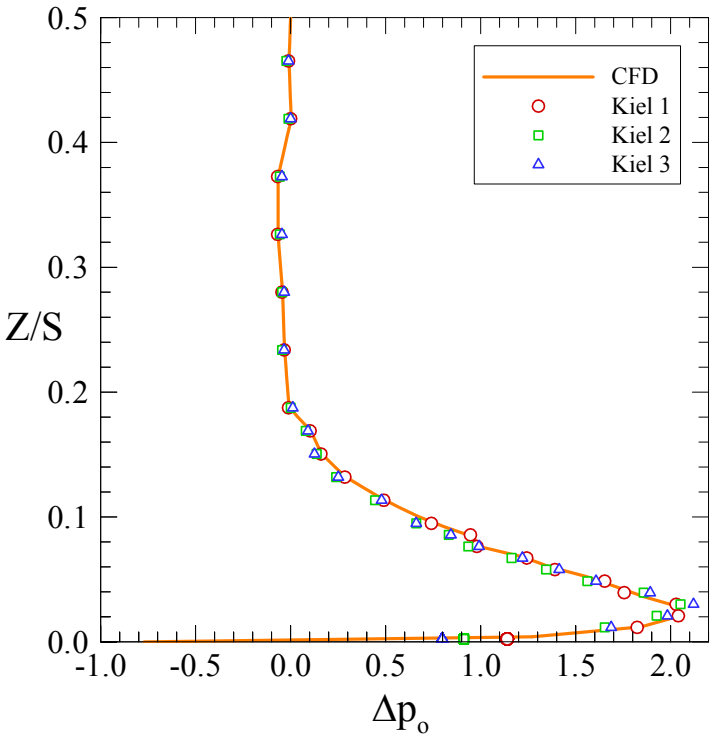

Figure 3.20 Inlet spanwise profile of normalized total pressure applied for fillet robustness computations (Case 4).

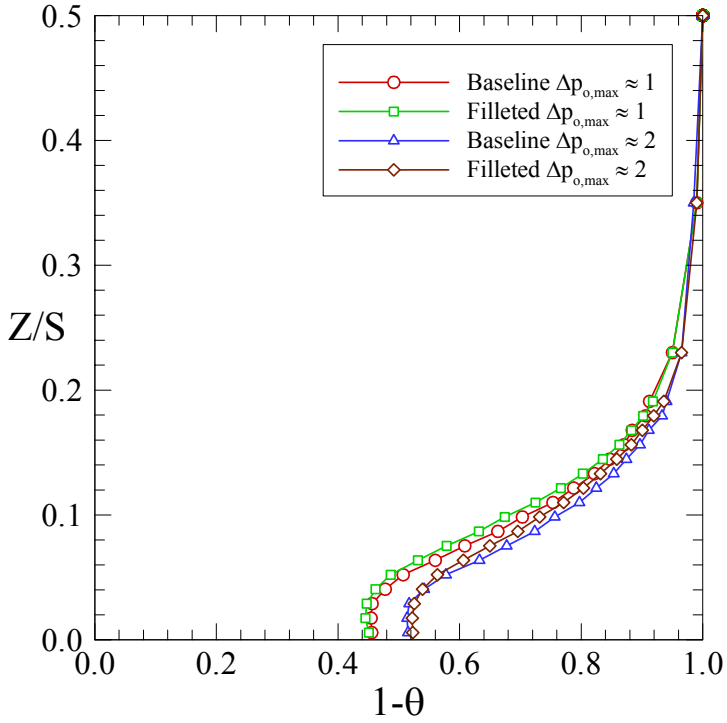

Figure 3.21 Comparison of the resultant inlet nondimensional temperature profiles for the two total pressure profiles considered (Cases 3 and 4).

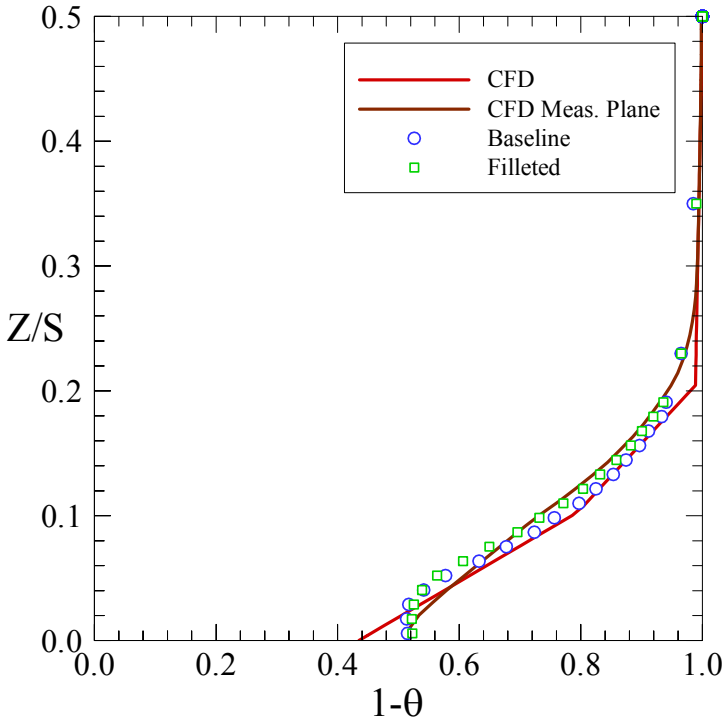

Figure 3.22 Inlet spanwise temperature profile applied for computations without the backward-facing slot (Case 4).

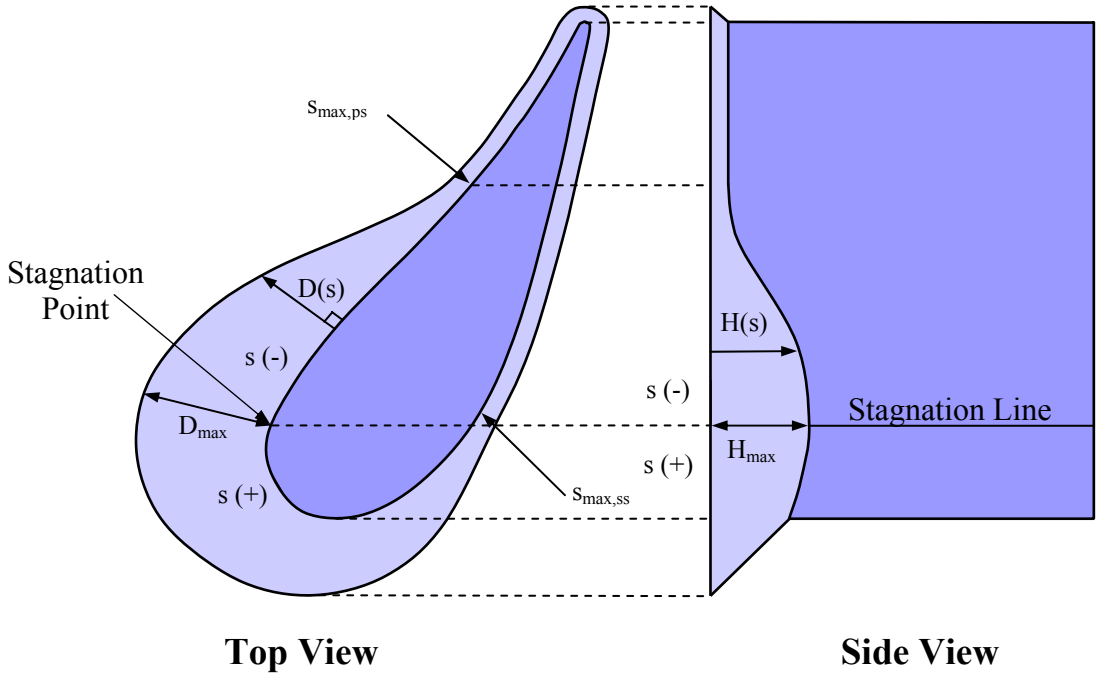

Figure 3.23 Leading edge fillet geometric model used in the preliminary fillet optimization with the location of H_{max} and D_{max} fixed at the vane dynamic stagnation.

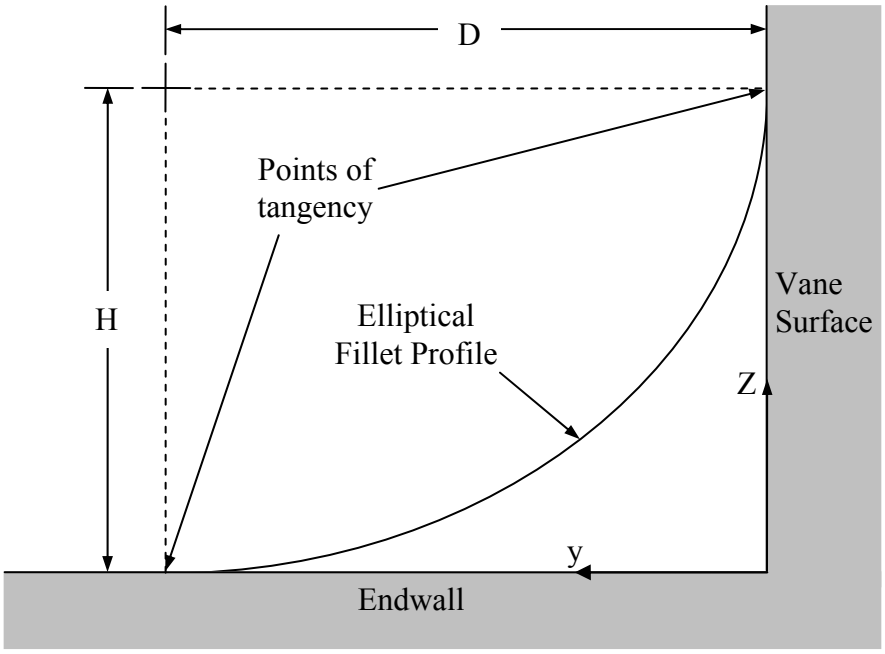

Figure 3.24 Elliptical fillet profile description.

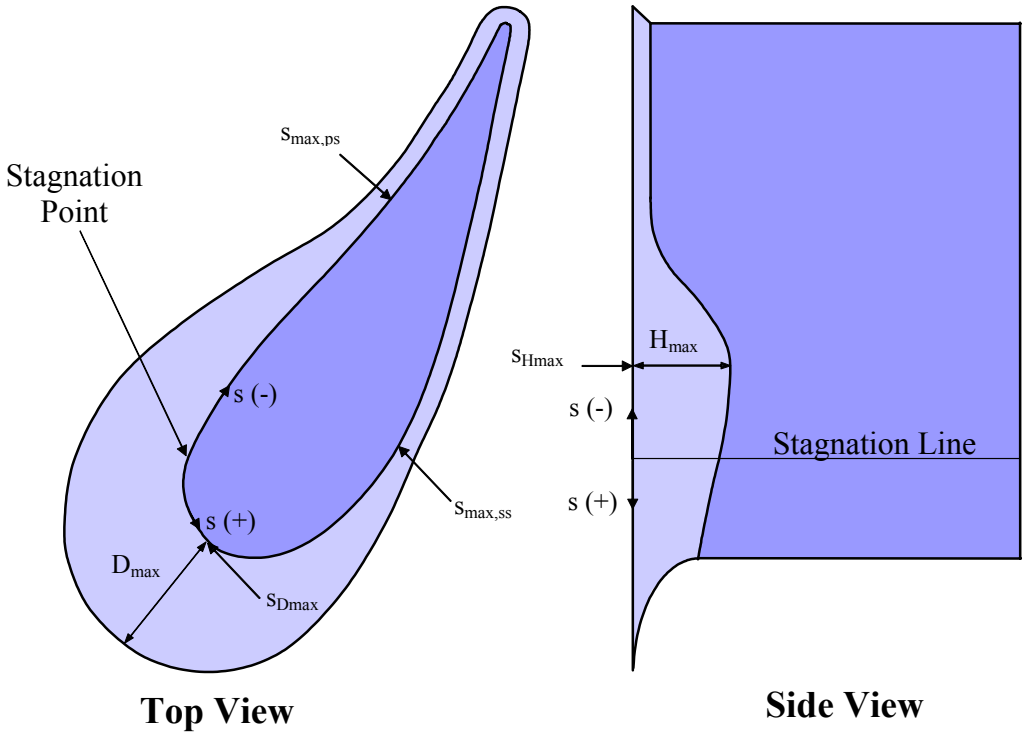

Figure 3.25 Illustration of a leading edge fillet with maximum fillet height and extent occurring along the pressure and suction surfaces, respectively.

Plane	s/C
SP	0.00
PS1	-0.16
PS2	-0.38
SS1	0.22
SS2	0.36
SS3	0.57

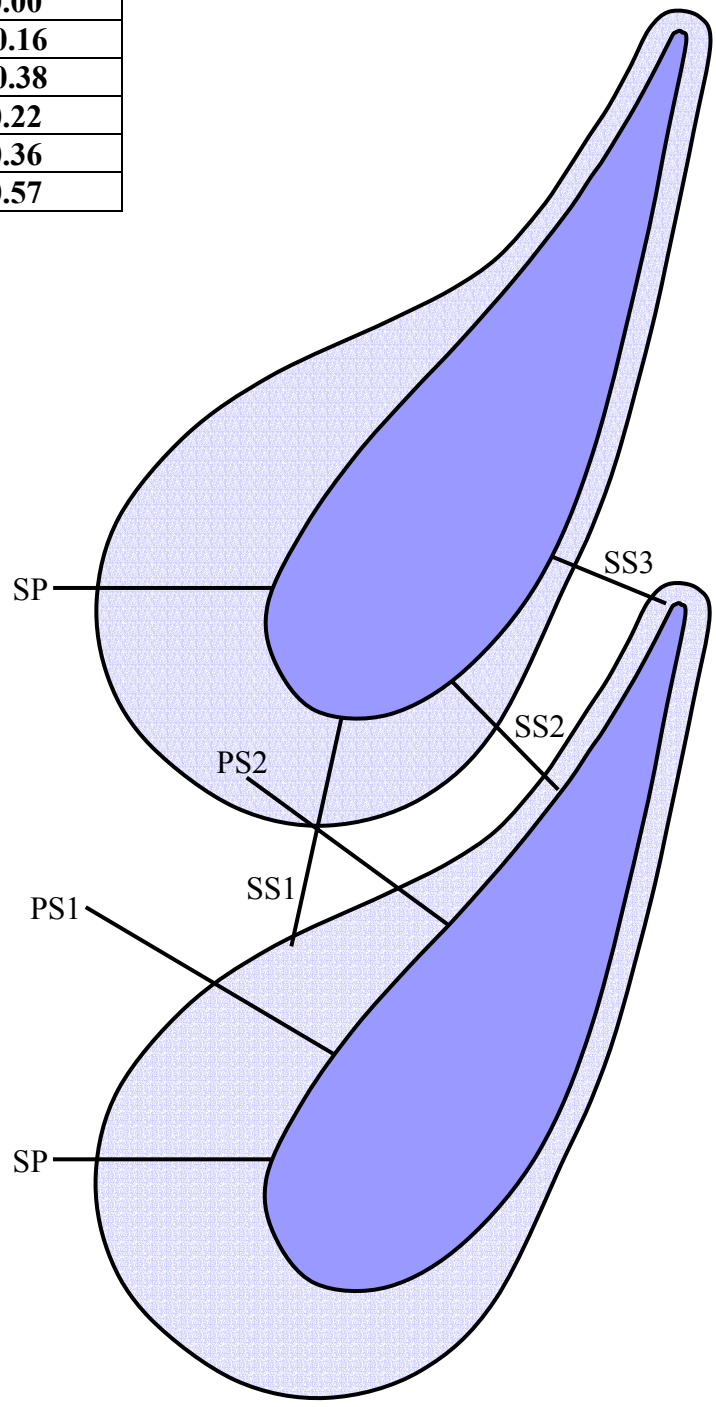

Figure 3.26 Locations of the flow analysis planes used to visualize the secondary flow field.

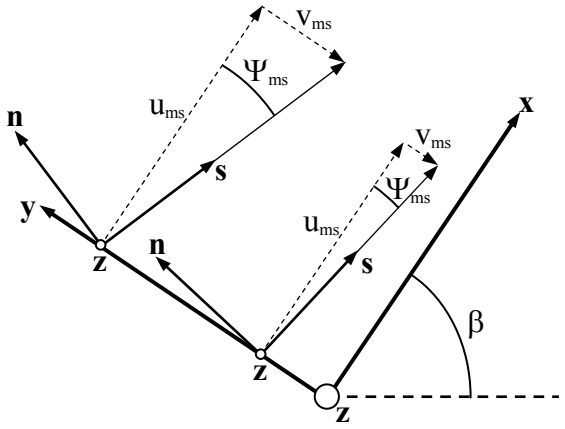

Note: Ψ_{ms} is a function of the distance from the vane surface, y. Therefore, coordinate directions **s** and **n** are also functions of y.

Calculation of the Midspan Flow Angle, Ψ_{ms}

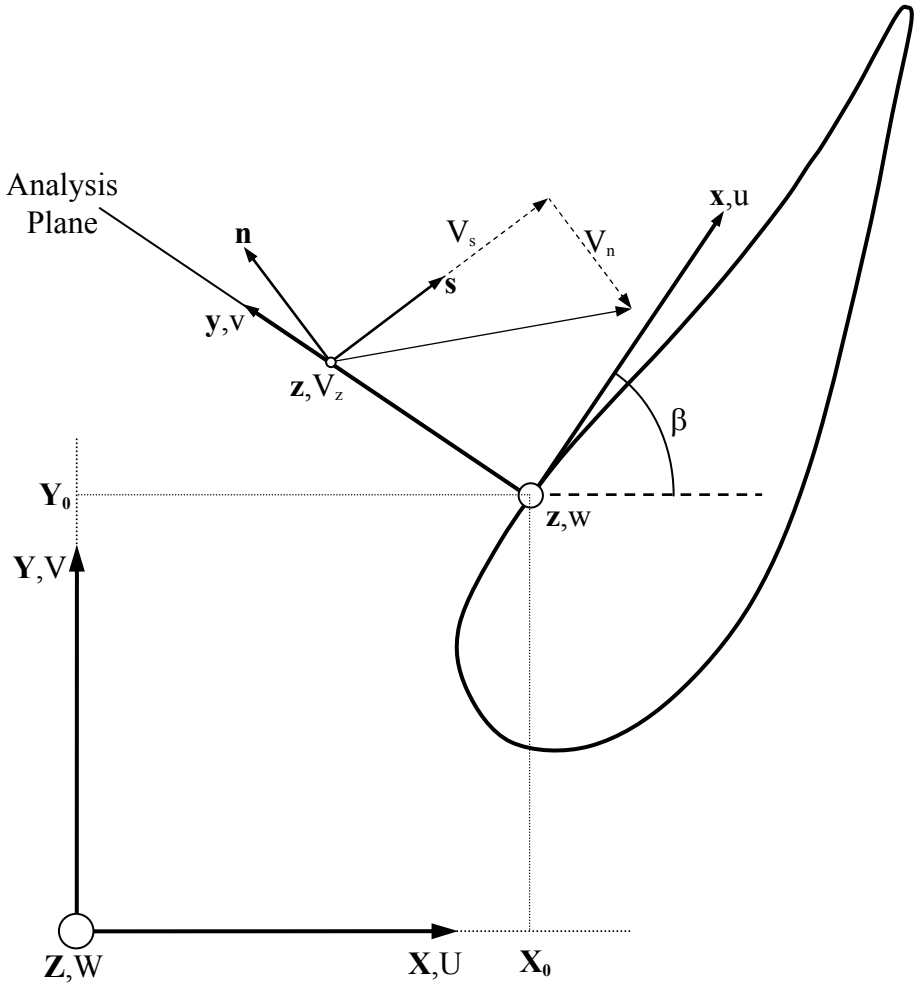

Figure 3.27 Velocity vector and coordinate transformations performed in calculation of the secondary flow field.